THE ASTROPHYSICAL JOURNAL, 551:1037–1064, 2001 April 20

HELIUM EMISSION FROM CLASSICAL T TAURI STARS: DUAL ORIGIN IN MAGNETOSPHERIC INFALL AND HOT WIND

GEORGINA BERISTAIN,[1] SUZAN EDWARDS,[1] AND JOHN KWAN
Five College Astronomy Department, Clark Science Center, Smith College, Northampton, MA 01063; sedwards@smith.edu, kwan@astro.umass.edu
Received 2000 September 10; accepted 2000 December 8

ABSTRACT

High-resolution emission-line profiles of He I and He II in 31 classical T Tauri stars are analyzed with the aim of probing the environs of the star-disk interface in accreting low-mass young stars. The diagnostic power of the helium lines lies in their high-excitation potentials, which restrict their formation to a region either of high temperature or close proximity to a source of ionizing radiation. The He I profiles are decomposed into kinematic components that support the paradigm of magnetically controlled accretion from the disk onto the stellar surface but also require a significant contribution from a hot wind. A *narrow component*, seen in 28/31 stars, is characterized by relatively uniform line widths and centroid velocities among all the helium lines. Our analysis supports previous conclusions that this feature is consistent with formation in the decelerating postshock gas at the magnetosphere footpoint. A *broad component*, seen in 22/31 stars, displays a diversity of kinematic properties. Our analysis suggests that in many stars the He I broad component is itself composite. At one extreme are stars where the broad component is redshifted in excess of 8 km s^{-1}, as would occur if helium emission arises primarily from polar angles less than 54°.7 in the funnel flow. At the other extreme are stars where the broad component is blueshifted in excess of -30 km s^{-1}, requiring an origin in outflowing gas. The additional occurrence of maximum blue wing velocities exceeding -200 km s^{-1} in 14 stars leads us to argue that hot winds are present in about half of our sample. The relation between the narrow component and the optical veiling differs between the stars with or without a hot helium wind, suggesting that when the hot wind is present the luminosity and temperature of the accretion shock are reduced. A comparison of broad component helium emission with standard outflow indicators leads us to suggest that there are two sources of inner wind in T Tauri accretion disk systems: one a hot polar/coronal wind that prevails in stars with high veiling, and the other a more widespread cool disk wind that is likely launched at the magnetosphere/disk boundary.

Subject headings: circumstellar matter — stars: pre–main-sequence — stars: variables: other — stars: winds, outflows

1. INTRODUCTION

As optically visible stars in the final stages of disk accretion, the classical T Tauri stars provide the opportunity to probe the interface between a young low-mass star and its accretion disk. This interface is controlled by a strong organized magnetosphere from the central star (Johns-Krull, Valenti, & Koresko 1999b; Guenther et al. 1999) that is capable of interrupting the disk and channeling disk material from the truncation region onto the star along closed field lines in a funnel flow (Uchida & Shibata 1985; Königl 1991; Hartmann, Hewett, & Calvet 1994, hereafter HHC94). Observational support for the ubiquity of funnel flows and accretion shocks on the stellar surface is summarized in Najita et al. (2000) and Edwards (1997). Coupling between the field and the disk may also affect the angular momentum evolution of the central star, regulating its spin while it actively accretes material from the inner disk (Königl 1991; Edwards et al. 1993a; Bouvier et al. 1993; Shu et al. 1994).

Although there are many aspects of funnel flows, accretion shocks, and stellar spin-down that are poorly understood and even controversial, one of the least understood aspects of the inner disk environment is the role, if any, that winds play in spinning down the star or transporting angular momentum from the inner disk (Shu et al. 2000; Königl & Pudritz 2000). The presence of energetic mass outflows on extended spatial scales in these systems is provided by lines of [O I], [S II], and [N II], which trace flows that have been collimated into jets and in some instances have been spatially resolved (Hirth, Mundt, & Solf 1997). An indication that winds are generated in near-stellar regions comes from the observation of blueshifted absorption features in a number of strong permitted lines, including Hα, Na D, Ca II, and Mg II. While the outer collimated wind, with a speed of ~200 km s^{-1}, is thought to originate close to the star (Kwan & Tademaru 1988), its connection with the inner wind traced by blueshifted absorption is not known, although both appear to be correlated with disk accretion rates, as diagnosed by continuum veiling or near-infrared excess (Hartigan, Edwards, & Ghandour 1995, hereafter HEG95; Calvet 1997; Najita et al. 2000).

High-resolution spectra offer the only means of exploring the nature of the elusive inner wind. However, the variety and complexity of the permitted line profiles in classical T Tauri star spectra present a formidable challenge to anyone seeking to understand the inner disk environment in these stars. Observed spectral features span a vast range in excitation and ionization potentials and differ markedly from one atomic species to another.

In this contribution we focus on optical lines of He I and He II as a probe of the star-disk interface. The diagnostic power of these lines lies in their high-excitation potential,

[1] Visiting Astronomer, Kitt Peak National Observatory, which is operated by AURA, Inc., under contract to the National Science Foundation.

which narrowly restricts the region in which they can form. This, coupled with the fact that He I λ5876 is one of the strongest and most prevalent permitted emission features in classical T Tauri star spectra, makes them an excellent candidate for detailed analysis. The lines of neutral and singly ionized helium require a strong ultraviolet flux or a high temperature for excitation, as their upper states lie $\sim$20 and 50 eV above the ground, respectively. If these lines are primarily collisionally excited, temperatures between 25,000 and 90,000 K are required (Athay 1965; Avrett, Vernazza, & Linsky 1976). With photoionization followed by recombination and cascade, helium excitation can take place at local kinetic temperatures between 8000 and 15,000 K (Zirin 1975; Heasley, Mihalas, & Poland 1974; Wahlstrom & Carlsson 1994).

Early investigations of He I and He II emission in classical T Tauri stars include (1) determination in two stars of the λ5876-to-λ6678 ratio (Schneeberger, Linsky, & Worden 1978); (2) comparison of the λ5876-to-λ10830 ratio in eight stars to wind, chromospheric, and nebular conditions (Ulrich & Wood 1981); and (3) estimation of a low optical depth for He II λ4686 based on the observed He II λ1640 luminosity in two stars (Lamzin 1989). Helium profiles in classical T Tauri stars can also be found in Boesgaard (1984), Appenzeller, Jankovics, & Jetter (1986), and Appenzeller, Reitermann, & Stahl (1988).

More recently, helium lines have been included in investigations of the kinematic properties of various permitted lines in classical T Tauri stars. Recognition that helium profiles, along with many other metallic features, appear composite with both narrow and broad kinematic components was pointed out by Hamann & Persson (1992) and Batalha et al. (1996). The narrow component (NC), characterized by line widths less than 50 km s^{-1} and centroid velocities close to the stellar velocity, has been attributed to formation in the postshock gas at the base of the funnel flow, although no detailed modeling of the line emission from this region has been attempted to date. The possibility that the broad component (BC) in metal lines arises in the accretion flow was investigated by Muzerolle, Hartmann, & Calvet (1998, hereafter MHC98), who found that they could reproduce line strengths and BC kinematics in Na D, Ca II, and O I in many, but not all, of the 11 stars they investigated. In particular, one example of a blueshifted centroid velocity in excess of what could be produced by a funnel flow and some redshifted emission centroids that were not explained by their models led MHC98 to suggest that a process other than magnetospheric accretion must contribute to the BC emission. Similar points were raised by Alencar & Basri (2000), who found that $\sim$20% of metallic BC profiles are redshifted by more than 5 km s^{-1}, in contradiction to the MHC98 models, which predict that emission lines formed along the length of infalling magnetospheric columns will have a blueward asymmetry.

Three studies have looked at the relation between the two kinematic components of metallic emission lines and the continuum veiling, which is the primary diagnostic of the disk accretion rate. In a study of 28 T Tauri stars, Batalha et al. (1996) reported correlations of the narrow and the broad component line strengths with the optical veiling, while in a variability study of the object DF Tau, Johns-Krull & Basri (1997) found a correlation between the BC emission and the veiling but did not find one for the NC. In their study of 11 classical T Tauri stars MHC98 found that metallic profiles dominated by NC emission tended to be from stars with low veiling and those dominated by BC emission tended to be from stars with high veiling.

In this paper we present an analysis of helium emission profiles in a sample of 31 classical T Tauri stars. The analysis is based on five helium lines extracted from a set of previously published red and blue echelle spectra, which were collected nonsimultaneously between 1988 and 1992. The He I triplet λ5876 and singlet λ6678 are taken from the red spectra, and He I triplets $\lambda\lambda$4471 and 4713 and He II λ4686 are taken from the blue spectra. The paper is organized as follows. The sample and data products are described in § 2. The decomposition of the profiles into two kinematic components (NC and BC) is described in § 3. A comparison of the ratios of NC and BC emission from simultaneously observed line pairs is presented in § 4. The kinematic properties of the NC and its likely formation in accretion shocks are discussed in § 5. The kinematic properties of the BC and its likely composite formation in funnel flows and hot inner winds are presented in § 6. The relations among the funnel flow, accretion shock, and hot wind and between them and the continuum veiling are discussed in § 7. In § 8 we explore the relation of the hot wind to other outflow indicators in classical T Tauri stars, and finally in § 9 we summarize our major conclusions and their implications for understanding disk accretion in low-mass young stars.

2. THE DATA

High-resolution spectra of 42 T Tauri stars were collected in seven observing runs with the KPNO 4 m Mayall telescope between 1988 and 1992. The He I and He II lines used in this investigation are extracted from these spectra, which include coverage at either red, $\sim$5000–6800 Å, or blue, $\sim$4000–4950 Å, wavelengths, taken nonsimultaneously. These spectra have been used in previous investigations of line profiles in T Tauri stars, including an examination of the relation of mass outflow and disk accretion (Edwards, Ray, & Mundt 1993b); a study of Balmer, Na D, and He I lines as indicators of magnetospheric accretion (Edwards et al. 1994); a study of forbidden lines as tracers of jets and possibly disk winds (HEG95); and an examination of Fe lines in DR Tau (Beristain, Edwards, & Kwan 1998). Details of the observing and data reduction can be found in some of the earlier papers. As in the previous papers, all profiles shown here are residual profiles, where an artificially veiled photosphere of a standard with the same spectral type as the target object has been subtracted from the observed spectrum (Hartigan et al. 1990). The veiling, r, is defined simply as the ratio of $F_{\rm veil}/F_{\rm phot}$, and it is determined separately for red and blue spectral regions. It ranges from values as high as 20 to as low as 0.1 for the classical T Tauri stars. The veiling continuum fluxes are the prime means of estimating disk mass accretion rates, with corresponding values of $\dot{M}_{\rm acc}$ ranging from $\sim 10^{-7}$ to 10^{-9} $M_\odot$ yr^{-1} (Gullbring et al. 1998).

We note that the generation of residual emission profiles by the subtraction of a synthetically veiled weak T Tauri star template assumes that the three contributions to the observed spectrum (photosphere, continuum veiling, and emission lines) combine in an additive manner. We find that the empirical justification for this assumption is strong in that (1) in stars with high veiling the subtraction process in a region with heavily veiled but still detectable photospheric

features leaves a featureless residual spectrum, and (2) in stars with low veiling the subtraction process in a region with an emission line whose wings are distorted by lightly veiled photospheric features leaves a residual profile with very smooth wings.

The sample of 42 T Tauri stars includes both (1) 32 classical T Tauri stars, with reddening corrected $(K-L)_o > 0.30$, veiling at $\lambda = 5700$ Å(r_R) or $\lambda = 4500$ Å$(r_B) > 0.1$, and detectable [O I] λ6300 ($W_\lambda > 0.1$ Å); and (2) 10 weak T Tauri stars, with reddening corrected $(K-L)_o < 0.30$ and no detectable veiling or [O I] λ6300 emission. Most of the stars have spectral types of late K or early M, although there are a few early K and mid M stars. We have omitted one classical T Tauri star from the original sample, RY Tau (spectral type K1), since it exhibits He I λ5876 in absorption, so that this paper relies on a sample of 31 classical T Tauri stars. Each star was observed at least once in the red, with between two and five multiple observations of 16 classical T Tauri stars. In the blue, only 16 classical T Tauri stars and one weak T Tauri star were observed at least once, with between two and five multiple observations of six classical T Tauri stars. The dates of the observations can be found in tables in Edwards et al. (1994) and HEG95.

The helium lines investigated here include two He I lines from the red spectra, the triplet λ5876 and singlet λ6678, plus three lines from the blue spectra, He I triplets $\lambda\lambda$4471 and 4713 and He II λ4686. The three triplet lines, $\lambda\lambda$5876, 4471 and 4713, arise from levels 3 ^3D, 4 ^3D, and 4 ^3S, with energies at 23.07, 23.73, and 23.59 eV above the ground level and radiative rates of $A = 7.1 \times 10^7$, 2.5×10^7, and 1.1×10^7 s^{-1}, respectively. The λ6678 singlet line arises from the 3 ^1D level at 23.07 eV, with $A = 6.4 \times 10^7$ s^{-1}. The one He II transition observed, λ4686, arises from the $n = 4$ level at 50.80 eV above the ground level with $A = 1.4 \times 10^8$ s^{-1}. Given the large energy differences between the excited states and the ground state in He I and He II, the most efficient way to populate these states is by electron capture and cascade following ionization. Insight into the physical conditions in the line formation region can be gleaned from triplet-to-singlet ratios, which will be examined in § 4.

Of the five helium lines in our spectra, the strongest is He I λ5876. It is seen in emission in all 31 of the classical T Tauri stars, with equivalent widths ranging from 0.1 to 7 Å, and in three of 10 weak T Tauri stars, with equivalent widths less than 0.2 Å. The next strongest is He I λ6678, which is seen in emission in 28/31 classical T Tauri stars and none of the weak T Tauri stars, with a maximum equivalent width of 2 Å. In the blue, He I λ4471 is found in all 16 classical T Tauri stars with blue spectra, with equivalent widths ranging from 0.1 to 1.4 Å. Of the other two blue lines, He I λ4713 is found in 10/16 classical T Tauri stars, with a maximum equivalent width of 0.4 Å, and He II λ4686 is found in 11/16 classical T Tauri stars, with a maximum equivalent width of 0.6 Å. The one weak T Tauri star with a blue spectrum, Lk Ca 7, shows no helium lines in emission or absorption. All equivalent widths are measured against the observed continuum, which includes both the photosphere and the veiling.

3. He I λ5876 LINE PROFILES AND DECOMPOSITION INTO NARROW AND BROAD COMPONENTS

He I λ5876 profiles are shown for the 31 classical T Tauri stars and three weak T Tauri stars in our sample in Figures 1*a* and 1*b*. The illustrated profiles are arranged in order of line width, from broadest to narrowest FWHM. We refer to this selection of profiles as the "reference sample." For stars with multiple observations, the profile in the reference sample is the one with the broadest FWHM. For classical T Tauri stars residual profiles are corrected for the veiled photosphere using artificially veiled spectral templates that had no λ5876 emission, and for weak T Tauri stars the original profiles with no veiling corrections are shown. A wide range of He I profile morphologies is apparent. Following MHC98, we can subdivide the 31 classical T Tauri star profiles into three classes: broad ($N = 3$), composite ($N = 19$), and narrow ($N = 9$). The three weak T Tauri stars with helium emission all fall into the narrow classification. What follows will be a discussion of the classical T Tauri star profiles, although we will include a comparison of the weak T Tauri star profiles in § 5, which focuses on the kinematics of the narrow component.

A visual comparison of the three morphology classes is made in Figure 2, where all profiles in a given class from the reference sample are normalized to their peak intensity. In the right panel a superposition of each individual profile is shown, and in the left panel the average profile for each class is presented. Figures 1 and 2 illustrate that the narrow core in the 19 composite profiles has an essentially identical structure to the nine profiles classified as narrow; together this is aptly identified as the *narrow component* (NC; Hamman & Persson 1992). In contrast, the *broad component* (BC) exhibits a considerable range in its kinematic properties, but its tendency *on average* to exhibit a blueward asymmetry is apparent in Figure 2. Although the BC is not detectable in any of the individual classical T Tauri star λ5876 profiles classified as "narrow," a weak blue-shifted BC is revealed in the average of these nine profiles, indicating that it is probably present in a significantly reduced strength most of the time.

In order to obtain a quantitative characterization of the He I profiles, the narrow and broad groups were fitted with a single-Gaussian function and the composite group with a double-Gaussian function. The relative amplitude, width, and centroid of each Gaussian are the undetermined parameters. Fits are optimized by minimizing the χ^2 statistic, and uncertainties in the parameter estimates are calculated by inverting the curvature matrix of the χ^2 function evaluated at the best-fit parameter set (Press et al. 1992). The resulting formal errors in the estimates rarely exceed 10% except in a few objects with weak emission and low signal-to-noise ratio (S/N), where the errors may reach 20%–30%.

The component fits are superposed on the observed λ5876 profiles of the reference sample in Figures 1*a* and 1*b*. For most profiles, both components are well described by Gaussians, although BC wing asymmetries are present in some stars (e.g., DG Tau). These asymmetries will be examined in § 6; in this section we simply use the Gaussian fits to distinguish the general behavior of the two kinematic components.

Kinematic properties of the λ5876 components are listed in Table 1 for all 66 observations of 31 classical T Tauri stars and illustrated in Figure 3 for the 31 classical T Tauri stars in the reference sample. The table lists centroid velocities, FWHM, and the extreme blueward velocity, evaluated at the zero intensity level in the blue wing, for all observations of all stars. The figure illustrates the dispersions in centroid velocity and FWHM for the selection of 31 refer-

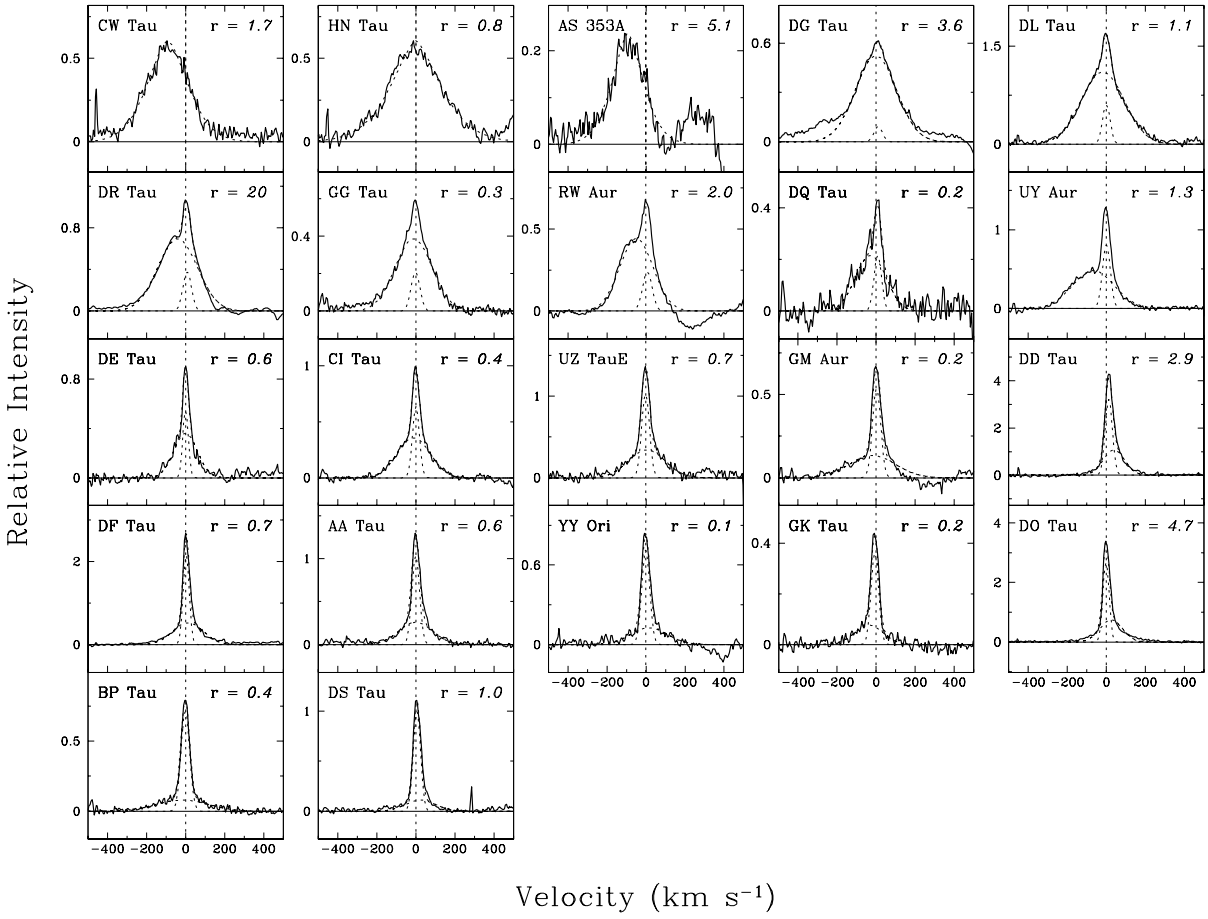

Fig. 1*a*

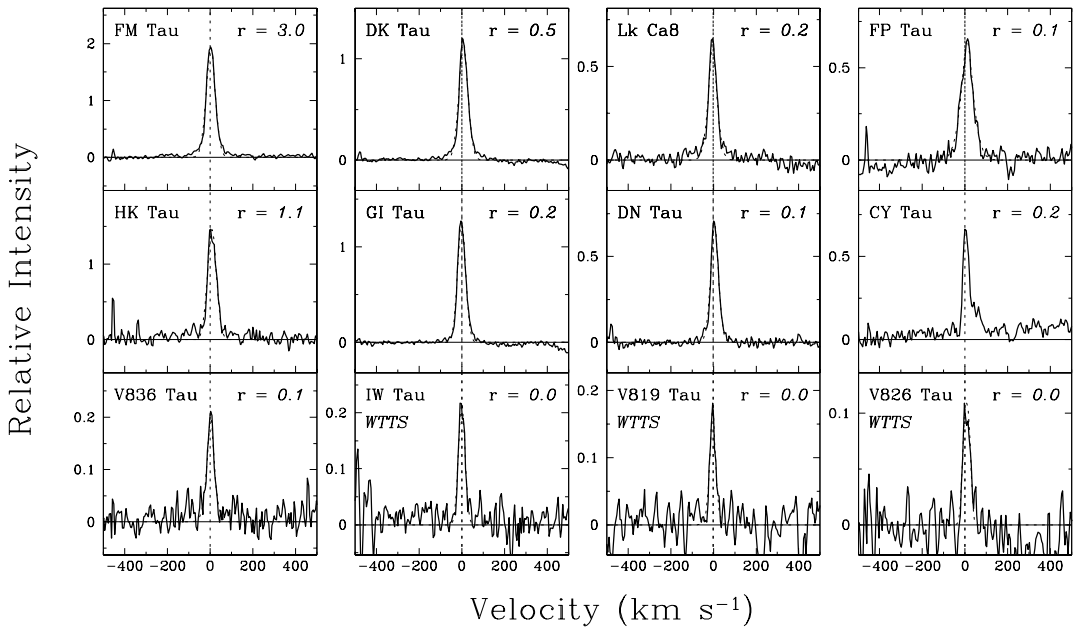

Fig. 1*b*

FIG. 1.—(*a*) Residual He I λ5876 profiles for the 22 classical T Tauri stars from the reference sample that have detectable BC emission, including three objects with BC-only profiles and 19 with composite (BC + NC) profiles. The simultaneous optical continuum veiling, *r*, is identified. Intensities are in units of the local continuum level, and velocities are with respect to the stellar photosphere. (*b*) Same as (*a*), but for the nine classical T Tauri stars from the reference sample that have NC-only emission at λ5876, plus three of 10 weak T Tauri stars with detectable λ5876 emission.

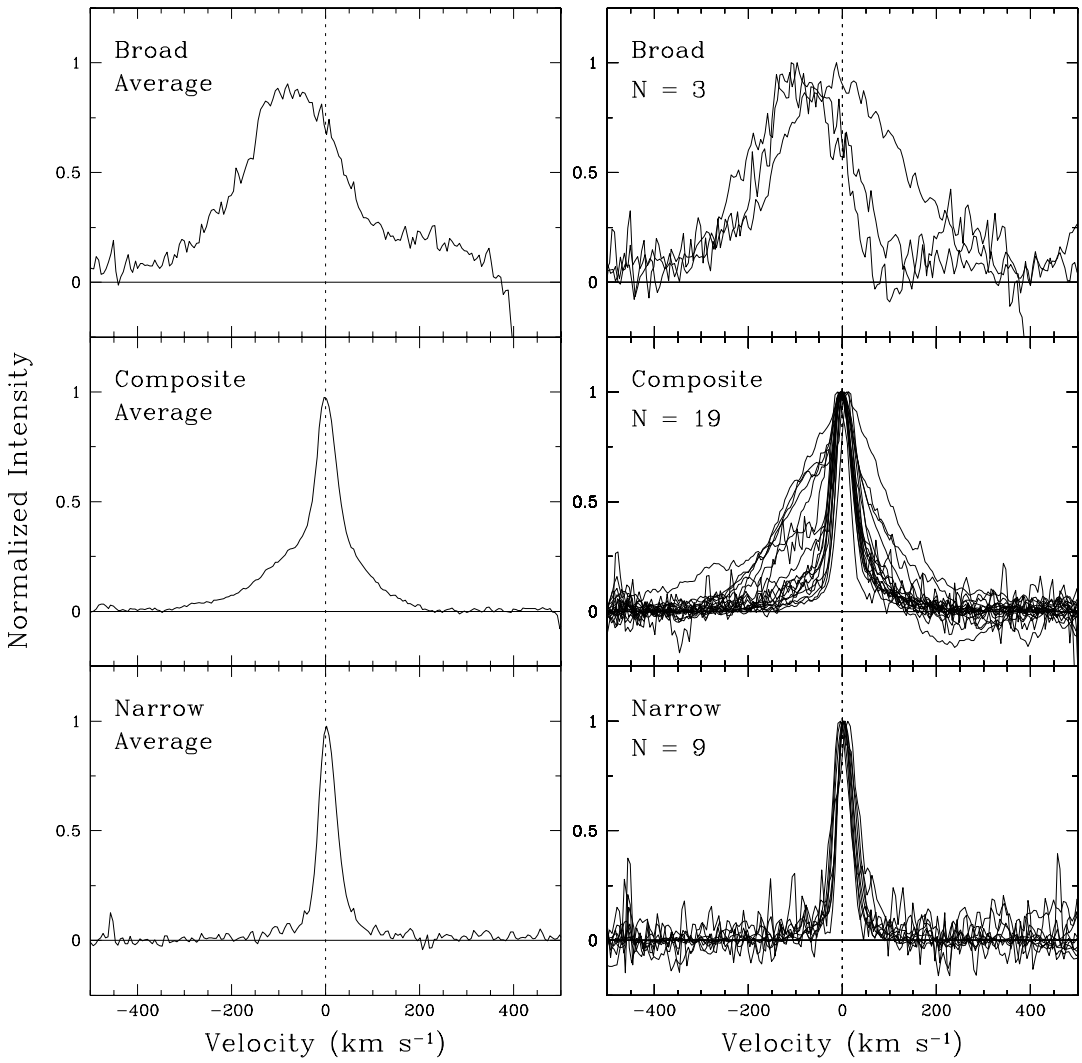

FIG. 2.—Comparison of the three morphological profile types: BC-only, composite (NC + BC), and NC-only profiles for He I λ5876 for the 31 classical T Tauri stars in the reference sample. Individual profiles in each category, normalized to their peak intensity, are superposed in the right panel. An average profile for each category is shown in the left panel. The narrow core in the composite profiles has identical kinematic properties as the NC-only profiles, indicating that they are the same feature.

ence sample profiles from Figure 1, revealing distinctive kinematic differences between the NC and BC. The NC has a narrow dispersion both in line width, with FWHM = 47 ± 7 km s^{-1}, and in its centroid velocity, with an average value of 5 ± 4 km s^{-1} relative to the stellar velocity (errors are standard deviations in the observed values). In contrast, the BC exhibits a considerable dispersion in each of these properties, with line widths ranging from about 130 to 300 km s^{-1} and centroid velocities ranging from a maximum blueshift of about −90 km s^{-1} to a maximum redshift of 35 km s^{-1} among the reference sample profiles in Figure 1.

The equivalent widths of λ5876 and related ratios are given for all observations of all stars in Table 2. In Figure 4 we present the relation between the equivalent width of each component and the simultaneously derived veiling, r_R, for the full data set, including multiple observations of the same star. We have adopted the approach of plotting line strengths as veiling-corrected equivalent widths, $W_\lambda(1 + r)$, which will be proportional to the line flux (Johns-Krull & Basri 1997). Although this approach can induce a correlation between these two observed quantities, it is revealing here in that we find that the veiling-corrected equivalent widths of the two components relate to the veiling in *different* ways. Specifically, we find that the BC flux increases proportionately with the veiling, but no strong correspondence between NC flux and veiling is apparent.

We reiterate that there is a wide range in the relative contribution to the total profile from the two components. The relative contributions are quantified by the ratio of equivalent widths, BC/NC, also listed in Table 2. The two extremes, three stars with only BC emission and nine stars with only NC emission, have already been mentioned. Among the 19 stars with measurable λ5876 emission in both the NC and BC, profiles range from those where the bulk of the helium emission is in the BC (five stars where BC/NC $\gtrsim$ 5) to those where the major contributor is the NC (six stars where BC/NC < 1). The ratio BC/NC is not well correlated with the veiling, but it will be shown to be related to kinematic properties of the BC in § 6.

One- or two-component Gaussian fits were also performed for the other four helium lines in our spectra. Both

TABLE 1

HE I λ5876 KINEMATICS OF NC AND BC

Object	r_R [a]	μ_{NC} (km s^{-1})	FWHM$_{NC}$ (km s^{-1})	μ_{BC} (km s^{-1})	FWHM$_{BC}$ (km s^{-1})	V_{bwing} (km s^{-1})
AA Tau	0.2	−3	38	...	...	...
	0.3	0	44	...	...	...
	0.6*	3	46	3	204	−200
AS 353A	5.1*	...	...	−93	182	−425
BP Tau	0.4*	1	52	−15	275	−335
	0.6	2	44	2	270	−200
	0.6	−3	45	...	...	...
CI Tau	0.4*	4	42	−8	200	−220
	0.5	−4	44	−4	214	−230
CW Tau	1.7*	...	...	−86	238	−360
CY Tau	0.2*	5	37	...	...	...
DD Tau	2.9*	7	42	32	128	−175
DE Tau	0.6*	−2	34	−2	142	−175
DF Tau	0.5	1	40	25	125	−250
	0.7*	5	37	14	185	−300
	1.6	7	44	57	164	−150
DG Tau	2.0	13	53	<7 (−68)	210	−650
	3.0	8	54	< −14 (−56)	206	−600
	3.6*	13	52	<2	248	−650
DK Tau	0.5*	8	47	...	...	...
DL Tau	1.1*	−1	48	−20	261	−370
	1.4	2	43	−9	250	−425
	2.1	6	44	−11	258	−400
	2.4	6	48	−2	237	−350
DN Tau	0.1*	7	41	...	...	...
DO Tau	4.7*	0	42	35	234	−200
DQ Tau	0.2*	4	46	−32	184	−200
	0.2	−3	44	15	224	−200
DR Tau	6.4	5	42	−18	224	−325
	9.2	4	48	−35	218	−400
	10	4	44	−18	252	−350
	20*	8	52	−41	238	−500
DS Tau	1.0*	6	44	24	182	−200
FM Tau	3.0*	3	49	...	...	...
	3.2	4	49	...	...	...
FP Tau	0.1*	16	68	...	...	...
	0.1	−1	74	...	...	...
	0.2	0	68	...	...	...
	0.2	...	...	...	...	...
GG Tau	0.1	−1	54	−25	234	−350
	0.3*	1	54	−9	222	−400
	0.5	2	56	−16	228	−400
GI Tau	0.2*	2	44	...	...	...
GK Tau	0.2*	−4	46	−35	172	−220
GM Aur	0.2*	3	50	−20	279	−320
	0.2	2	50	−25	252	−300
HK Tau	1.1*	17	49	...	...	...
HN Tau	0.8*	...	...	0	287	−400
LK Ca8	0.1	3	39	...	...	...
	0.1	4	41	...	...	...
	0.2*	2	43	...	...	...
	0.2	−2	43	...	...	...
RW Aur	1.7	3	64	−63	238	−350
	1.8	−7	56	−39	274	−450
	1.8	2	54	−2	230	−300
	2.0*	6	58	−50	202	−275
UY Aur	0.2	−2	46	...	...	...
	0.3	0	54	−78	286	−375
	0.4	9	38	8	152	−275
	0.6	12	42	7	213	−325
	1.3*	0	48	−67	252	−325
UZ TauE	0.7*	0	48	6	222	−200
V836 Tau	<0.1	−3	33	...	...	...
	0.1*	3	36	...	...	...

TABLE 1—*Continued*

Object	r_R[a]	μ_{NC} (km s^{-1})	FWHM$_{NC}$ (km s^{-1})	μ_{BC} (km s^{-1})	FWHM$_{BC}$ (km s^{-1})	V_{bwing} (km s^{-1})
	0.1	0	41	...	...	...
YY Ori.....	0.1*	7	48	24	222	−175

NOTE.—Errors in μ, the centroid velocity, are typically 2 km s^{-1} for the NC and 5 km s^{-1} for the BC. Errors for the FWHM are typically a few kilometers per second for the NC and 10 km s^{-1} for the BC. V_{bwing} is the BC blue wing velocity at zero intensity; uncertainties are typically 30 km s^{-1}. The double-Gaussian fitting procedure for DG Tau gives only lower limits to μ_{BC}, as a result of the extended blue BC wing and blueshifted absorption. An estimate of μ_{BC} for the unattenuated BC can be obtained for two of the three epochs ($r_R = 2$ and 3) by fitting the wings of the residual BC profile outside the interval affected by absorption with a single-Gaussian function. The results of such fits are given in parentheses for DG Tau.

[a] The veiling at 5200 Å; an asterisk indicates the reference sample.

BC emission and NC emission are seen in the other three He I lines, but only NC emission is seen in He II. Of the 28/31 classical T Tauri stars with He I λ6678 emission, the NC is present in 24 stars and the BC in 13. Equivalent widths and ratios of BC/NC for λ6678 are given in Table 2. The other helium line where BC emission is common is He I λ4471. This line is detected in all 16 classical T Tauri stars in our blue sample, with 13 cases showing NC emission and 12 showing BC emission. The equivalent widths for this feature are given in Table 3, both for the total line and the NC. However, since λ4471 BC emission is usually blended with strong BC from neighboring Ti II λ4468 just 208 km s^{-1} to the blue of the helium line, we only use the NC, which appears to be reliably extracted in the fitting procedure, in our subsequent analysis. Equivalent widths for the other two blue helium lines are also given in Table 3. He I λ4713 is detected in 10/16 stars and He II λ4686, which is always NC only, in 11/16 stars. The kinematic properties for the NC in all five helium lines are summarized in Table 4.

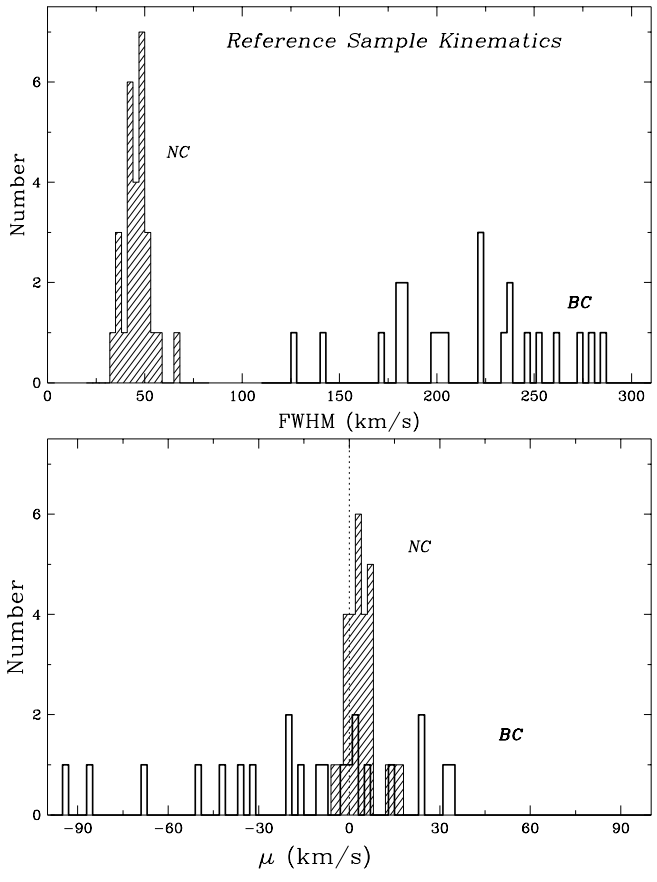

FIG. 3.—Comparison of the distribution of FWHM and of centroid velocity, μ, for the two kinematic components of He I λ5876 for the 31 classical T Tauri stars in the reference sample. Both parameters are derived from unconstrained single- or double-Gaussian fits to the residual profiles. The NC, found in 28 stars, exhibits uniform FWHM and centroid velocity whenever it is observed. In contrast, the BC, seen in 22 stars, exhibits considerable dispersion in both kinematic parameters.

In this section we have illustrated the general characteristics of the NC and BC for λ5876 using parameters derived from the two-component fits. In the next two sections we continue to investigate properties of the NC and BC using the fit parameters. However, in § 6, in order to investigate the kinematic properties of the BC in more detail, we abandon the fit parameters for λ5876 and instead construct residual BC profiles by subtracting off the emission from the NC fits to all composite profiles.

4. COMPONENT INTENSITY RATIOS

In the previous section we demonstrated that the NC and BC have distinctive kinematic properties in He I λ5876. In this section we demonstrate that these two components are characterized by differences in their triplet-to-singlet ratio, $I_{\lambda 5876}/I_{\lambda 6678}$, clarifying that they arise in regions of differing physical conditions.

Under nebular conditions λ5876 emission is stronger than λ6678. Level populations for pure recombination and cascade in the limit of very low electron densities, where collisional excitation from the metastable 2 ^3S and 2 ^1S is ignored, result in a triplet-to-singlet ratio of $I_{\lambda 5876}/I_{\lambda 6678} \sim 3.5$ (Brocklehurst 1972; Smits 1996). The triplet-to-singlet ratio will initially increase with increasing density. For example, if the effects of collisional excitation are included from the highly metastable 2 ^3S level for λ5876 ($A = 1.3 \times 10^{-4}$ s^{-1}) and from the metastable 2 ^1S level for λ6678 ($A = 51$ s^{-1}), then at densities of $10^2 \leq N_e \leq 10^6$ cm^{-3} and a temperature of $T_e = 20 \times 10^3$ K the $I_{\lambda 5876}/I_{\lambda 6678}$ ratio is raised to 5.1 (Smits 1991). At densities so high that collisional de-excitation of λ5867 begins to compete with radiative decay, collisions will provide coupling between the singlet and triplet levels, allowing the transfer of population between the two spin systems and driving the $I_{\lambda 5876}/I_{\lambda 6678}$ ratio toward its thermal equilibrium value near unity.

We can evaluate the triplet-to-singlet ratio of $I_{\lambda 5876}/I_{\lambda 6678}$ for 24 classical T Tauri stars in the NC and for 13 classical T Tauri stars in the BC. In the absence of flux-calibrated spectra we simply use the ratio of observed equivalent widths for each component. For comparison we

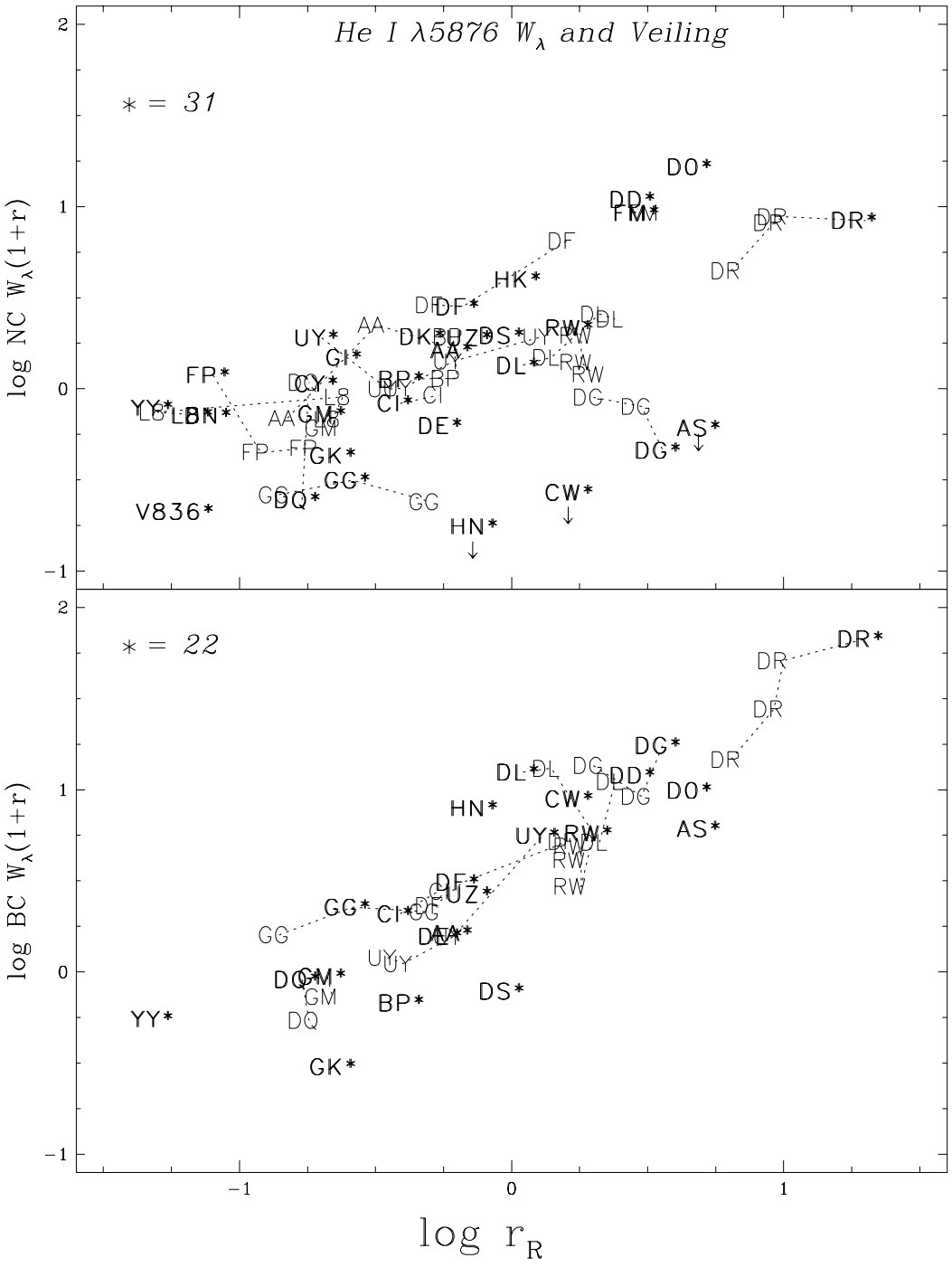

FIG. 4.—Comparison of the relation between veiling-corrected equivalent width and veiling for each kinematic component of He I λ5876, with NC in the upper panel and BC in the lower panel. In each case, all observational epochs are included in the figure, with multiple observations of a given star connected by a dashed line. The parameters from the reference sample, whose profiles appear in Figs. 1 and 2, are designated by an asterisk, and the number of objects from the reference sample in each panel is also identified. It is seen that there is a different relation between line flux and veiling for the NC compared to the BC, with a clear proportionality between these quantities for the BC but little correspondence between them for the NC.

note that over this 800 Å region the continuum ratio for a 4000 K blackbody is ~0.9 and a 10^4 K blackbody, which is more appropriate for a star that is heavily veiled, has a ratio of 1.4. The triplet-to-singlet ratios for the NC and the BC emission are given in the last two columns of Table 2 and shown in Figure 5.

It is seen that the NC triplet-to-singlet ratio is relatively uniform among all 24 classical T Tauri stars, with a mean and standard deviation of 2.0 ± 0.6. The fact that this is almost a factor of 2 below the value for nebular recombination is best explained by line formation under conditions of high density and near thermal equilibrium. In contrast, although the BC triplet-to-singlet ratio is subject to more uncertainty, its mean value of 3.4 ± 1.5 is significantly closer to the nebular value, suggesting that on average it comes from a region of lower density than that of the NC.

We can also compare NC ratios among the blue lines, found in Table 3, to those expected for nebular conditions

TABLE 2

W_λ AND COMPONENT RATIOS FOR RED He I LINES

		He I λ5876			He I λ6678				
OBJECT	r_R	W_λ(total)	W_λ(NC)	BC/NC	W_λ(total)	W_λ(NC)	BC/NC	NC (5876/6678)	BC (5876/6678)
AA Tau.....	0.2	0.6	0.6	<0.1	0.2	0.1	<0.1	4.1 (0.7)	...
	0.3	1.7	1.7	<0.1	0.8	0.8	<0.1	2.1 (0.1)	...
	0.6*	2.0	1.0	1.0	0.6	0.6	<0.1	1.6 (0.1)	...
AS 353A.....	5.1*	0.9	<0.1	>9	0.9	<0.1	>9	...	1.0 (0.2)
BP Tau	0.4*	1.2	0.8	0.6	0.4	0.4	<0.1	1.8 (0.3)	...
	0.6	1.2	0.7	0.6	0.3	0.3	<0.1	2.2 (0.3)	...
	0.6	1.2	1.2	<0.1	0.4	0.4	<0.1	2.8 (0.2)	...
CI Tau.....	0.4*	2.0	0.6	2.5	0.8	0.3	1.4	1.9 (0.2)	3.3 (1.3)
	0.5	2.5	0.6	3.0	0.5	0.5	<0.1	1.2 (0.2)	...
CW Tau	1.7*	3.1	<0.1	>31	0.6	<0.1	>6	...	5.3 (1.5)
CY Tau.....	0.2*	0.9	0.9	<0.1	<0.03	...	...	...	...
DD Tau	2.9*	6.0	2.8	1.1	2.1	1.2	0.8	2.4 (0.2)	3.5 (0.8)
DE Tau.....	0.6*	1.4	0.4	2.5	0.3	0.3	<0.1	1.2 (0.2)	...
DF Tau.....	0.5	3.5	1.9	0.8	0.7	0.7	<0.1	2.8 (0.2)	...
	0.7*	3.6	1.7	1.1	1.2	0.6	0.7	2.8 (0.1)	3.2 (1.0)
	1.6	4.4	2.5	0.8	1.4	1.4	<0.1	1.7 (0.1)	...
DG Tau	2.0	5.3	0.3	15.1	0.9	<0.1	>15	...	6.1 (1.1)
	3.0	2.7	0.2	11.5	1.1	0.1	8.2	1.8 (1.0)	2.5 (0.6)
	3.6*	3.5	0.1	38.1	1.1	<0.1	>18	...	3.3 (0.5)
DK Tau	0.5*	1.3	1.3	<0.1	0.6	0.6	<0.1	2.4 (0.1)	...
DL Tau.....	1.1*	6.6	0.6	9.3	1.8	0.3	5.1	2.1 (0.4)	3.9 (0.8)
	1.4	6.2	0.6	8.8	1.7	0.3	4.7	2.1 (0.3)	3.9 (0.6)
	2.1	2.5	0.8	2.0	1.1	0.4	1.4	2.2 (0.4)	2.3 (1.1)
	2.4	4.0	0.7	4.6	1.2	0.4	2.1	1.8 (0.2)	4.0 (0.7)
DN Tau	0.1*	0.7	0.7	<0.1	0.3	0.3	<0.1	2.3 (0.2)	...
DO Tau	4.7*	4.6	2.9	0.6	1.7	1.2	0.4	2.4 (0.1)	3.2 (0.9)
DQ Tau	0.2*	1.0	0.2	3.7	<0.03	...	...	...	...
	0.2	1.4	0.9	0.5	0.5	0.5	<0.1	1.9 (0.2)	...
DR Tau	6.4	2.6	0.6	3.3	1.0	0.3	1.7	1.8 (0.1)	3.3 (0.3)
	9.2	3.5	0.8	3.4	1.4	0.5	2.0	1.7 (0.1)	2.9 (0.5)
	10	5.3	0.8	5.8	2.0	0.5	2.6	1.5 (0.1)	3.2 (0.3)
	20*	3.9	0.4	8.0	2.0	0.4	4.1	1.1 (0.1)	2.2 (0.3)
DS Tau	1.0*	1.4	1.0	0.4	0.5	0.5	<0.1	1.9 (0.1)	...
FM Tau	3.0*	2.3	2.3	<0.1	0.8	0.8	<0.1	2.8 (0.2)	...
	3.2	2.2	2.2	<0.1	<0.9	<0.9	...	...	...
FP Tau	0.1*	1.1	1.1	<0.1	<0.2	<0.2	<0.1	...	...
	0.1	0.4	0.4	<0.1	<0.03	...	...	...	...
	0.2	0.4	0.4	<0.1	<0.03	...	...	...	...
	0.2	<0.4	<0.4	...	<0.03	...	...	...	...
GG Tau	0.1	1.5	0.2	6.1	0.3	<0.1	>2.1	...	6.7 (4.0)
	0.3*	2.1	0.2	7.2	0.4	0.1	2.5	2.1 (0.4)	6.1 (2.4)
	0.5	1.6	0.2	8.9	<0.3	<0.3	...	...	...
GI Tau	0.2*	1.2	1.2	<0.1	0.6	0.6	<0.1	2.1 (0.1)	...
GK Tau	0.2*	0.6	0.3	0.7	0.2	0.2	<0.1	1.5 (0.2)	...
GM Aur.....	0.2*	1.3	0.6	1.3	0.6	0.6	<0.1	1.0 (0.1)	...
	0.2	1.1	0.5	1.2	0.6	0.6	<0.1	0.9 (0.2)	...
HK Tau	1.1*	1.9	1.9	<0.1	0.7	0.7	<0.1	2.8 (0.6)	...
HN Tau	0.8*	3.8	<0.1	>38	1.3	<0.1	>13	...	2.9 (1.6)
LK Ca8.....	0.1	0.7	0.7	<0.1	0.2	0.2	<0.1	3.9 (1.2)	...
	0.1	0.7	0.7	<0.1	0.2	0.2	<0.1	3.2 (0.8)	...
	0.2*	0.7	0.7	<0.1	0.2	0.2	<0.1	3.0 (0.6)	...
	0.2	0.6	0.6	<0.1	0.2	0.2	<0.1	3.1 (0.7)	...
RW Aur	1.7	2.4	0.8	1.9	1.3	0.5	1.6	1.7 (0.1)	2.1 (0.3)
	1.8	2.3	0.7	2.5	1.2	0.2	4.0	2.8 (0.3)	1.8 (0.3)
	1.8	1.7	0.5	2.1	0.8	0.3	1.6	1.7 (0.1)	2.3 (0.4)
	2.0*	2.1	0.4	4.8	1.5	0.1	10.0	2.6 (1.1)	1.2 (0.3)
UY Aur.....	0.2	1.6	1.6	<0.1	0.7	0.7	<0.1	2.3 (0.1)	...
	0.3	1.6	0.7	1.2	0.6	0.4	0.5	1.9 (0.1)	4.3 (1.8)
	0.4	1.5	0.7	1.1	0.6	0.6	<0.1	1.3 (0.1)	...
	0.6	1.9	0.9	1.1	0.6	0.6	<0.1	1.6 (0.1)	...
	1.3*	3.3	0.8	2.9	1.1	0.4	1.6	2.0 (0.2)	3.7 (1.0)
UZ TauE.....	0.7*	2.6	1.1	1.4	0.5	0.5	<0.1	2.2 (0.5)	...
V836 Tau.....	<0.1	0.1	0.1	<0.1	<0.03	...	...	...	...
	0.1*	0.2	0.2	<0.1	<0.03	...	...	...	...

TABLE 2—*Continued*

		He I λ5876			He I λ6678				
OBJECT	r_R	W_λ(total)	W_λ(NC)	BC/NC	W_λ(total)	W_λ(NC)	BC/NC	NC (5876/6678)	BC (5876/6678)
	0.1	0.2	0.2	<0.1	<0.03	...	...	...	...
YY Ori.....	0.1*	1.3	0.8	0.7	0.5	0.5	<0.1	1.5 (0.4)	...

NOTE.—W_λ in Å are with respect to the total (photospheric + veiling) continuum. Asterisks denote the reference sample, and uncertainties for the triplet-to-singlet component ratios are in parentheses.

for 11 classical T Tauri stars. For the blue He I triplet pair, $I_{\lambda4471}/I_{\lambda4713}$, the mean value is 6.0 ± 3.4, which is somewhat below the prediction of 9.8 (Smits 1991). For the He I–to–He II ratio, $I_{\lambda4471}/I_{\lambda4686}$, the observed NC ratios have a mean value of 1.7 ± 1.1, in comparison to the published nebular recombination value of $I_{\lambda4471}/I_{\lambda4686} = 0.04(N_{\mathrm{He}+}/N_{\mathrm{He}++})$ (Osterbrock 1974). If the lines are due purely to recombination and cascade, a range of $N_{\mathrm{He}+}/N_{\mathrm{He}++}$ between 19 (DR Tau) and 104 (UY Aur) would bring the theoretical ratios into agreement with the observed ones. However, the He II $n = 4$ level has, besides the λ4686 transition to $n = 3$, a λ1215.1 transition to $n = 2$. Since the latter line is only 0.6 Å away from the wavelength of hydrogen Lyα, expected to be very strong and broad in classical T Tauri stars, the absorption of Lyα by He II $n = 2$ will likely contribute substantially to the observed He II λ4686 intensity in classical T Tauri stars.

5. KINEMATICS OF THE NARROW COMPONENT: ORIGIN IN POSTSHOCK GAS

The line width and centroid velocities of the NC emission can be compared for all five helium lines in our spectra. The

TABLE 3

W_λ AND RATIOS FOR BLUE HELIUM LINES

Object	r_B[a]	He I λ4471 W_λ(total)[b]	He I λ4471 W_λ(NC)[c]	He I λ4713 W_λ(total)[d]	He II λ4686 W_λ(total)[e]	NC (4471/4713)[f]	NC (4471/4686)[g]
AA Tau	0.2	0.9	0.5	0.1	0.2	4.0 (1.9)	2.2 (0.8)
	0.2*	1.0	0.4	0.2	0.5	2.3 (1.0)	0.9 (0.2)
AS 353A.....	5.1*	3.1	<0.1	<0.1	<0.1	...	...
BP Tau.....	0.6	1.2	0.7	0.1	0.5	7.4 (4.6)	1.3 (0.3)
	0.8	1.0	0.4	<0.1	< 0.5	...	0.9 (0.4)
	1.0*	1.0	0.7	0.1	0.5	5.4 (2.2)	1.4 (0.7)
CW Tau.....	0.9*	1.8	<0.1	<0.1	<0.1	...	...
DF Tau	1.8*	2.1	1.2	0.3	0.5	4.6 (1.0)	2.5 (0.6)
	4.3	2.3	1.4	0.3	0.4	4.9 (1.2)	3.1 (0.5)
	7.3	1.1	1.0	0.2	0.2	6.3 (1.9)	4.2 (1.2)
	7.5	0.9	0.7	0.1	0.2	5.6 (2.2)	3.4 (1.1)
	9.1	0.8	0.4	0.1	0.2	3.3 (0.7)	2.1 (0.7)
DG Tau	5.6*	3.9	<0.1	<0.1	<0.1	...	...
DK Tau	0.6*	1.0	0.5	0.1	0.6	4.5 (1.8)	0.9 (0.1)
DL Tau	5.7*	3.7	0.3	0.2	0.5	1.3 (0.5)	0.6 (0.3)
DN Tau	0.1*	0.7	0.6	0.1	0.2	8.8 (5.6)	2.6 (0.8)
	0.1	0.6	0.5	<0.1	0.2	...	...
	0.3	0.6	0.6	<0.1	< 0.3	...	...
DR Tau	8.1*	1.7	0.4	0.1	0.5	2.9 (0.5)	0.8 (0.1)
	8.9	3.8	0.3	0.4	0.5	0.8 (0.4)	0.7 (0.3)
	13	1.6	0.3	0.1	0.4	2.0 (0.4)	0.6 (0.1)
DS Tau.....	1.9*	1.1	0.7	0.1	0.4	5.5 (1.8)	1.7 (0.2)
GG Tau	0.3*	1.2	0.1	<0.1	<0.1	...	...
GK Tau	0.3*	0.8	0.8	0.1	0.4	8.5 (6.1)	2.1 (0.5)
GM Aur.....	0.1*	0.5	0.4	<0.1	< 0.3	...	1.7 (0.9)
RW Aur	2.7	0.9	<0.4	0.1	0.4	<3.1	<0.9
	3.0	1.2	<1.0	0.1	0.3	<7.6	<2.9
	3.3	1.6	<0.6	0.1	0.4	<4.9	<1.3
	4.3*	0.4	0.1	<0.2	0.2	...	0.6 (0.4)
	9.9	0.1	0.1	<0.2	<0.2	...	...
UY Aur	0.5*	1.1	1.0	0.1	0.2	13.0 (4.8)	4.2 (0.9)

NOTE.—W_λ in Å are with respect to the total (veiling + photospheric) continuum.

[a] The veiling at 4500 Å. An asterisk indicates the blue reference sample used in compiling statistics of the blue NC properties.

[b] The total equivalent width for λ4471, which may include Ti II λ4468.4 as part of the BC. Errors are approximately 20%.

[c] The unblended NC equivalent width for λ4471. Errors are approximately 20%.

[d] The total equivalent width for He I λ4713. Errors in this weak line can be as large as 50%.

[e] The total equivalent width for He II λ4686. This line is NC only in all 11 stars where it is detected. Errors in this weak line can be as large as 50%.

[f] The ratio of NC equivalent widths for He I, $W_\lambda(4471)/W_\lambda(4713)$. Errors are in parentheses.

[g] The ratio of NC equivalent widths for He I to He II, $W_\lambda(4471)/W_\lambda(4686)$. Errors are in parentheses.

TABLE 4

NC KINEMATICS FOR ALL HELIUM LINES

ID	λ (Å)	N_{NC} [a]	$\mu \pm \sigma$ (km s^{-1})	FWHM $\pm \sigma$ (km s^{-1})
He I	5876	28	4 ± 5	47 ± 7
	6678	24	7 ± 6	37 ± 6
	4471	13	6 ± 3	37 ± 6
	4713	11	6 ± 4	34 ± 9
He II.....	4686	12	10 ± 5	52 ± 8

[a] The number of stars with NC helium emission out of 31 stars in the red and 16 in the blue.

NC average FWHM and centroid velocity for each helium transition are listed in Table 4, and their distributions are illustrated in Figure 6. Both the line widths and centroid velocities are found to be relatively uniform among all the NC helium features, although there are some small systematic differences in the mean values between lines. Mean line widths range from the broadest line, He II λ4686 with FWHM $= 52 \pm 8$ km s^{-1}, to the narrowest line, He I λ4713 with FWHM $= 34 \pm 9$ km s^{-1}. Similarly, all five helium lines tend to have average NC centroid velocities that are modestly redshifted relative to the stellar photospheric

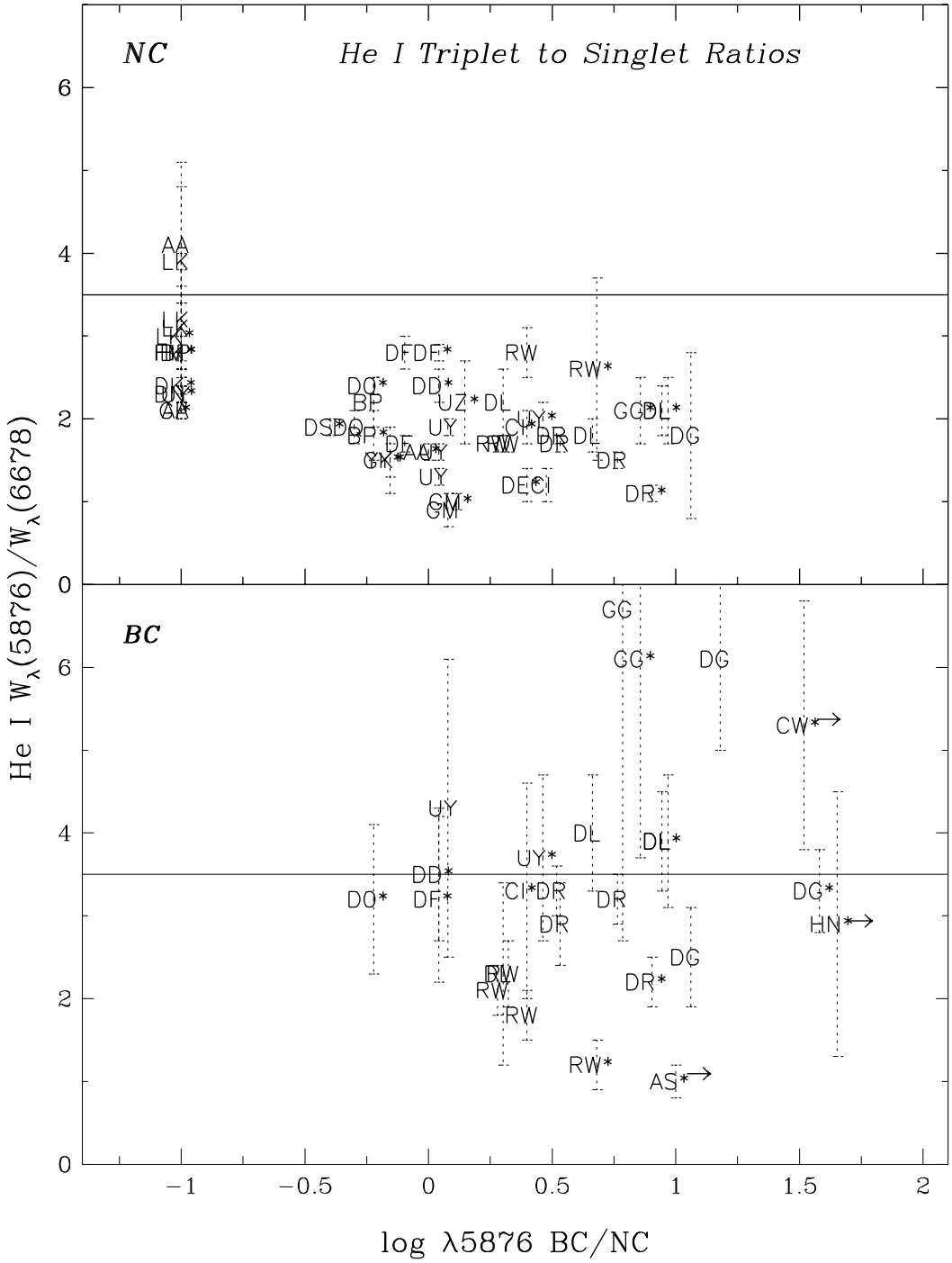

FIG. 5.—Comparison of the He I triplet-to-singlet ratio, $I_{\lambda 5876}/I_{\lambda 6678}$, for each kinematic component, with NC ratios in the upper panel and BC ratios in the lower panel. In each case, all observational epochs where a ratio can be determined are included, with the reference sample, whose profiles appear in Figs. 1 and 2, designated by an asterisk. The horizontal line in each panel represents the nebular ratio of 3.5

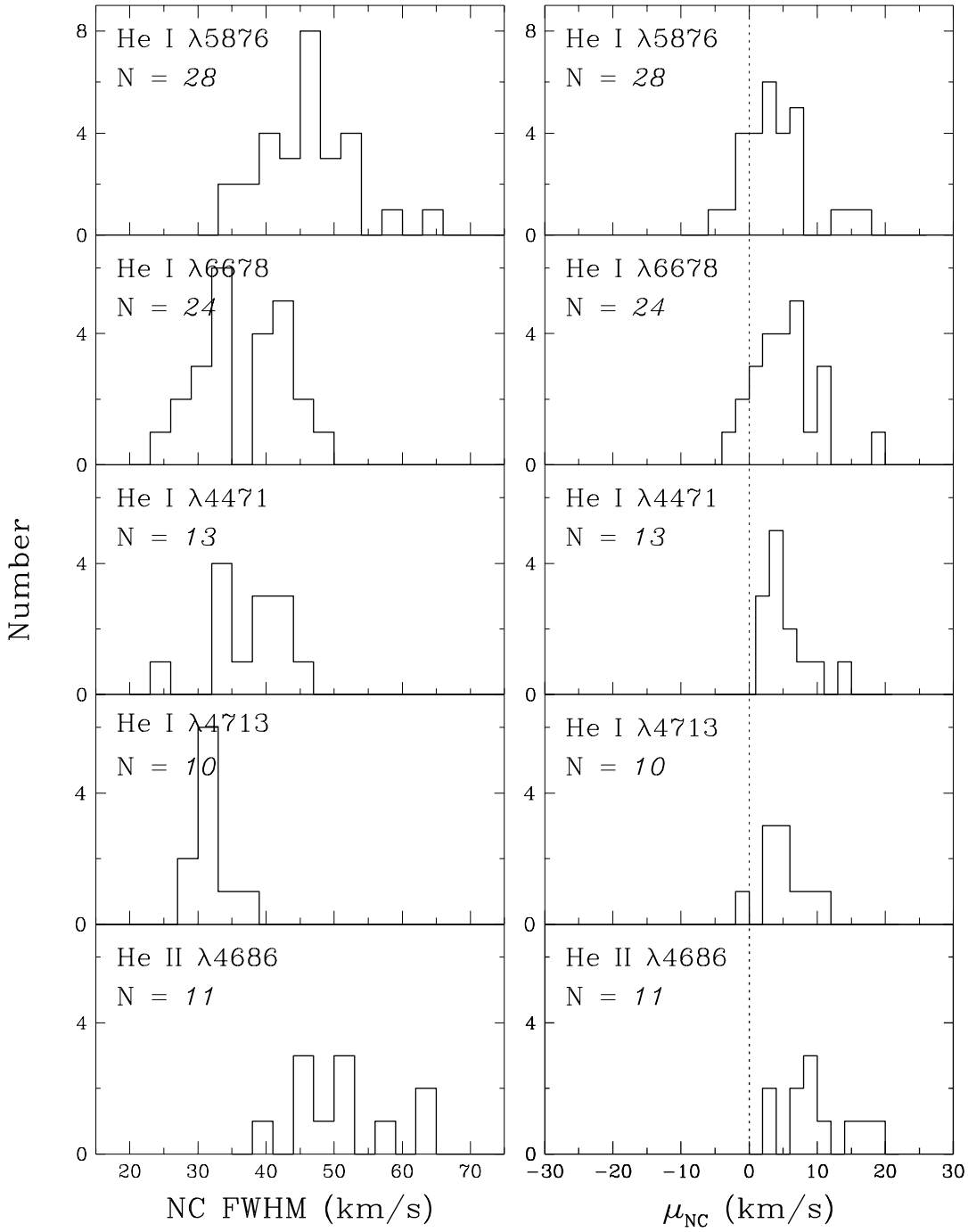

FIG. 6.—Distributions of the FWHM and centroid velocity, μ_{NC}, for NC emission of all five helium lines in our data: He I $\lambda\lambda$5876, 6678, 4472, 4713 and He II λ4686. The broadest NCs are $\lambda\lambda$5876 and 4686, and the narrowest is λ4713. All helium NC distributions have means that are slightly redshifted relative to the stellar velocity, with the largest, a mean redshift of 10 km s^{-1}, for λ4686.

velocity, with individual measurements ranging from -5 to 20 ± 5 km s^{-1}, and with He II λ 4686 having the largest average redshift of 10 ± 5 km s^{-1}.

The kinematic properties of the NC in He I and He II are most readily explained as originating in postshock gas at the base of magnetospheric accretion columns (Batalha et al. 1996; Calvet et al. 1996; Najita et al. 2000). The small redshifts indicate that helium lines originate in a region where the gas is still decelerating, and the larger line width and redshift for He II are consistent with λ4686 formation closer to the accretion shock, where the temperature, gas speed, and ionizing flux are all relatively higher. Additional evidence that helium lines arise in a magnetospheric accretion shock comes from the discovery of significant circular polarization in λ5876 NC emission in the classical T Tauri star BP Tau, indicating field strengths $\geq$2.4 kG in the NC line formation region (Johns-Krull et al. 1999a; Johns-Krull & Valenti 2000).

Although the properties of NC emission from other metallic lines have also been interpreted as arising in post-

shock gas, there is growing evidence that the NC kinematics can differ substantially in lines of different excitation energies. For example, we previously found that NC emission from 62 unblended Fe I and Fe II lines (with excitation potentials less than 6 eV) in the classical T Tauri star DR Tau, using the same spectra analyzed here for He I and He II, had an average FWHM of 22 ± 4 km s^{-1} and an average centroid velocity of -1 ± 2 km s^{-1} (Beristain et al. 1998). Similarly, we have examined the red spectra of our 31 classical T Tauri stars and found NC emission in both Fe II λ5363 (10 stars) and Mg I λ5184 (16 stars). The kinematic properties of the NC for these two lines in our full sample of stars are found to be very similar to those for the Fe I and Fe II lines in DR Tau, with an average FWHM of 27 ± 7 km s^{-1} and an average centroid velocity of -5 ± 5 km s^{-1} (the data are not shown here). The factor of 2 decrease in NC line width and the change from redshifted to stationary NC centroid velocities from He II/He I to Fe I/Mg I lines, as ionization potentials drop from 54 to 8 eV and excitation energies drop from 50 to 2 eV, suggest that it will be possible to compare postshock cooling models with NC emission properties.

We also note that three out of 10 of the weak T Tauri stars in our sample show weak NC emission in the strongest helium line, He I λ5876 ($W_\lambda < 0.2$ Å). The weak T Tauri stars, which lack continuum veiling, forbidden line emission, and near-infrared excess emission, are thought not to possess inner disks with active accretion or to drive energetic winds (HEG95). Although we have λ5876 detections in only three weak T Tauri stars, their properties appear to differ from the NC in the classical T Tauri stars in that (1) their equivalent widths are at least several times smaller than those for all but one classical T Tauri star (V836 Tau, an object with one of the lowest known accretion rates); (2) the line widths are 20% narrower on average, with a mean FWHM of 36 ± 6 km s^{-1}; and (3) the average centroid velocity, 1.3 ± 5.2 km s^{-1}, is not redshifted. Presumably the weak λ5876 emission in weak T Tauri stars can be attributed to an active chromosphere, which would be expected to be present in classical T Tauri stars as well, although its contribution would have a negligible effect on the determination of classical T Tauri star NC parameters in all but one star. Comparative studies of emission-line polarization in weak T Tauri stars and classical T Tauri stars coupled with synoptic spectroscopic monitoring of the radial velocity and line strength in weak T Tauri stars could be helpful in confirming a chromospheric origin for their weak NC helium emission.

6. KINEMATICS OF THE HELIUM BROAD COMPONENT: DUAL ORIGIN IN ACCRETION FLOW AND WIND

In contrast to the simple and uniform characteristics of the NC helium emission, the kinematic properties of the BC are complex and diverse. In Figure 7 we illustrate residual BC profiles derived by subtracting the NC Gaussian fits from the veiling-corrected total profiles, where each residual profile has been scaled to the peak of the BC emission. The selection of stars is identical to Figure 1*a*, representing the 22/31 classical T Tauri stars in the reference sample with BC λ5876 emission. The distributions of centroid velocity and FWHM for these 22 BC profiles were illustrated earlier in Figure 3 to demonstrate the distinctions between the BC and the NC. Here we look in more depth at the kinematic properties of the BC and include the statistics from all 43 observations of the 22 stars with BC emission. We note the following characteristics:

1. The BC centroid velocities (μ_{BC}) range from blueshifts as high as -93 km s^{-1} (CW Tau) to redshifts as high as 57 km s^{-1} (DF Tau; profile not shown). Among the reference sample (Fig. 7 profiles) BC blueshifts ≤ -8 km s^{-1} occur in 12/22 stars and redshifts ≥ 8 km s^{-1} in 5/22 stars. When multiple observations outside the reference sample are considered, the total number of stars that show blueshifts is 13 (DG Tau changes from a centered profile to a blueshifted one), and the number showing redshifts is seven (DQ Tau and UY Aur both change from blueshifted to redshifted BC emission during our observing period).
2. The extreme velocity in the blue wing ranges from -150 km s^{-1} to at least -600 km s^{-1}. It exceeds -200 km s^{-1} in 14/22 stars and exceeds -300 km s^{-1} in 11/22 stars.
3. The extreme velocity in the red wing has a much smaller range, from 140 to 300 km s^{-1}. It exceeds 200 km s^{-1} in only four objects.
4. Redshifted absorption below the continuum level at velocities between 150 and 400 km s^{-1} is seen in five stars in at least one observing epoch. Four are shown in Figure 7 (RW Aur, GK Tau, GM Aur, and YY Ori), and the other one (DR Tau) is seen in spectra outside the reference epoch. AS 353A may also have redshifted absorption, although the close proximity of the Na D lines with very strong and complex P Cygni profiles makes this identification tentative.

The high-velocity redshifted absorption features are most readily explained as arising in a magnetospheric accretion flow (HHC94) and are reminiscent of those seen in upper Balmer lines, Na D, Ca II, and O I λ7773 (Edwards et al. 1994; MHC98). It is likely that redshifted absorption that does not extend below the continuum may be present in other stars as well. In the remainder of this section we will argue that although magnetospheric infall is certainly indicated by the BC helium profiles in many stars, there is often an additional contributor to the profile, which we will argue is a hot wind. There are three observational phenomena we will use in this argument: the presence of blueshifted absorption in the helium BC in one star, the distribution of velocity centroids of the helium BC, and the maximum blue wing velocities of the helium BC.

The presence of a hot wind with some optical depth is clearly indicated in one star, DG Tau, which exhibits blueshifted absorption at λ5876 on two of three observational epochs. In Figure 8 we display all three of our He I λ5876 profiles for the high accretion rate star DG Tau and superpose the simultaneously observed Hα profile, with both normalized to their peak intensities. The helium lines are total profiles (including both NC and BC emission) and are displayed with a wider velocity range than the previous figures, extending to ± 900 km s^{-1}, in order to illustrate the similar velocity structure in the blue wing of each of these strong lines. It can be seen that on two of the three observing epochs Hα shows two distinct blueshifted absorption features that are usually attributed to formation in an inner wind. At both of those epochs, the simultaneous He I λ5876 shows an identical structure to Hα blueward of about -175 km s^{-1}, including a blueshifted absorption feature at approximately -200 km s^{-1} and blue wings extending out to at least -600 km s^{-1}. Although this is the only star

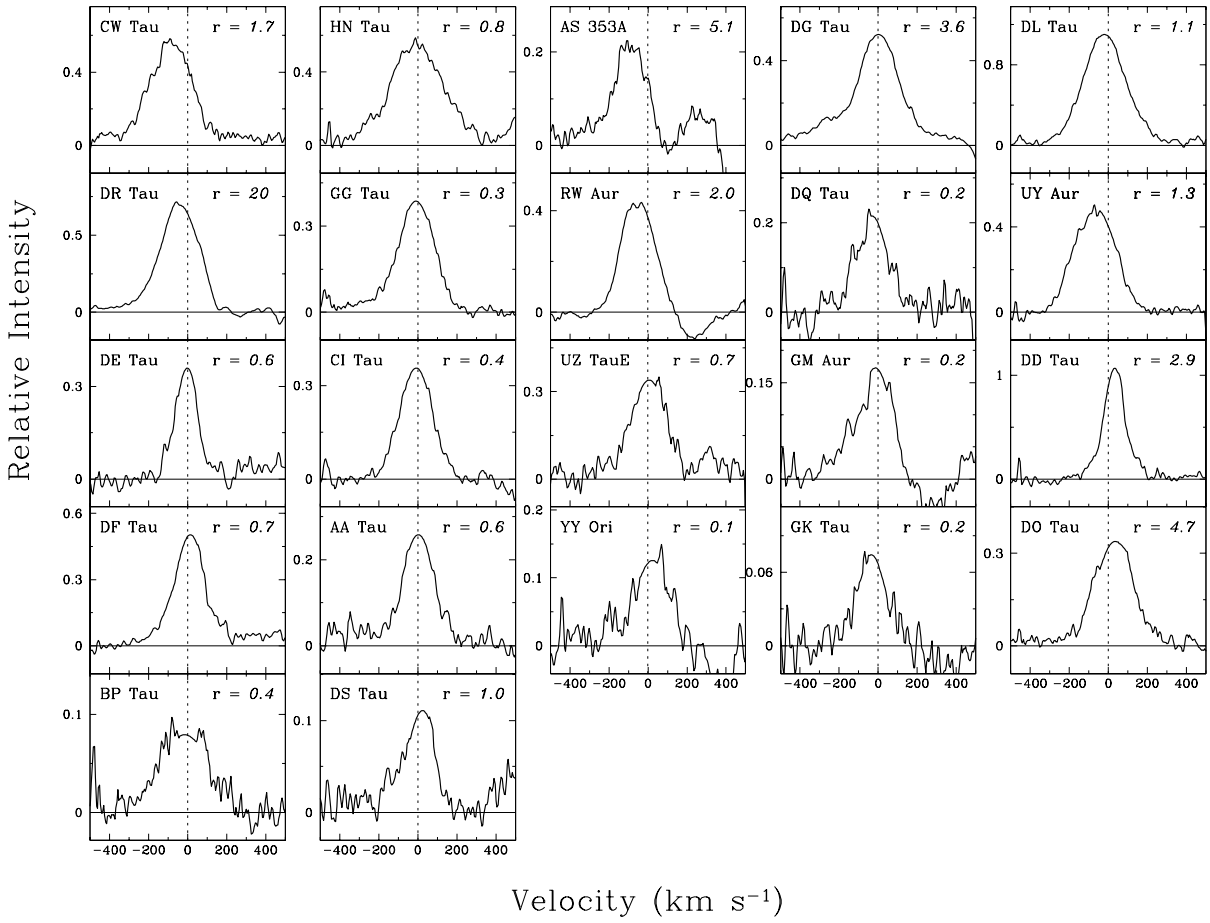

FIG. 7.—Residual BC He I λ5876 profiles for the 22 classical T Tauri stars from the reference sample with BC emission (Fig. 1*a*). For the 19 stars with composite λ5876 profiles the BC is generated by subtracting the NC, evaluated by a two-component Gaussian fit, from the total profile. Each profile has been normalized to the peak of the BC emission, and intensity units are relative to the local continuum.

where we see blueshifted absorption in λ5876, it provides strong evidence for a hot inner wind in this object.

In the rest of this section we will focus on the centroid velocity and blue wing velocity of the helium BC emission and argue that this emission arises in part from infalling gas in the funnel flow that is close to the accretion shock and in part from a hot wind. Regarding the centroid velocity, we note that redshifted absorption from infalling magnetospheric gas cannot be invoked to produce blueshifted centroid velocities in excess of -30 km s^{-1}. Redshifted absorption, which is present in at least five of our stars, is formed when infalling gas absorbs continuum photons from a hot zone at the base of the magnetosphere, provided the inclination and line opacity are favorable (see HHC94). Its presence cannot produce an observed centroid as blue as -30 km s^{-1}. For example, the spectrum of RW Aur from the reference epoch shown in Figure 7 has a blueshifted BC centroid of -50 km s^{-1} and a prominent redshifted inverse P Cygni absorption at 250 km s^{-1}. Examination of the profile reveals that restoring the absorbed continuum flux will not significantly alter the blueshifted emission centroid. Thus, we must account for the centroid velocity of the BC by examining the conditions of the emitting gas.

We begin by examining the kinematic properties of emission lines formed in an optically thin idealized funnel flow. This allows us to place constraints on both the emission centroid and the maximum blue wing velocity for profiles formed under these conditions. We will then show that many of the observed BC helium profiles exceed these constraints and therefore cannot be accounted for solely with a funnel flow. Two of the velocity components of infalling gas in an axisymmetric, aligned, rigidly rotating dipolar magnetospheric funnel flow are v_z, the velocity perpendicular to the disk plane (along the symmetry axis), given by

$$v_z = v_p \frac{(3 \sin^2 \theta - 2)}{(1 + 3 \cos^2 \theta)^{1/2}} ,$$

and v_p, the poloidal velocity at polar angle θ, given by

$$v_p^2 = \frac{2GM_*}{R_*} \sin^2 \theta_0 \left(\frac{1}{\sin^2 \theta} - 1 \right) - \frac{R_*^2 \Omega_*^2}{\sin^4 \theta_0} (1 - \sin^6 \theta) ,$$

where θ_0 is the polar angle of the field line when it intersects the stellar surface. The root of v_z is at $\theta = \arcsin (2/3)^{1/2}$, so that a particle falling along a field line will have a positive v_z when it is at a polar angle $\theta > 54.^\circ7$ and a negative v_z at $\theta < 54.^\circ7$. These velocity components and the critical polar angle $\theta = 54.^\circ7$ are illustrated in Figure 9.

The magnetosphere can be thought of as a sequence of axisymmetric rings of successively smaller radii as the polar angle decreases from its value at the disk plane, $\theta = \pi/2$, to θ_0. The profile that would be generated by each axisymmetric ring of emitting particles above the disk plane is symmetric about a centroid velocity of $-v_z \cos i$, where i is

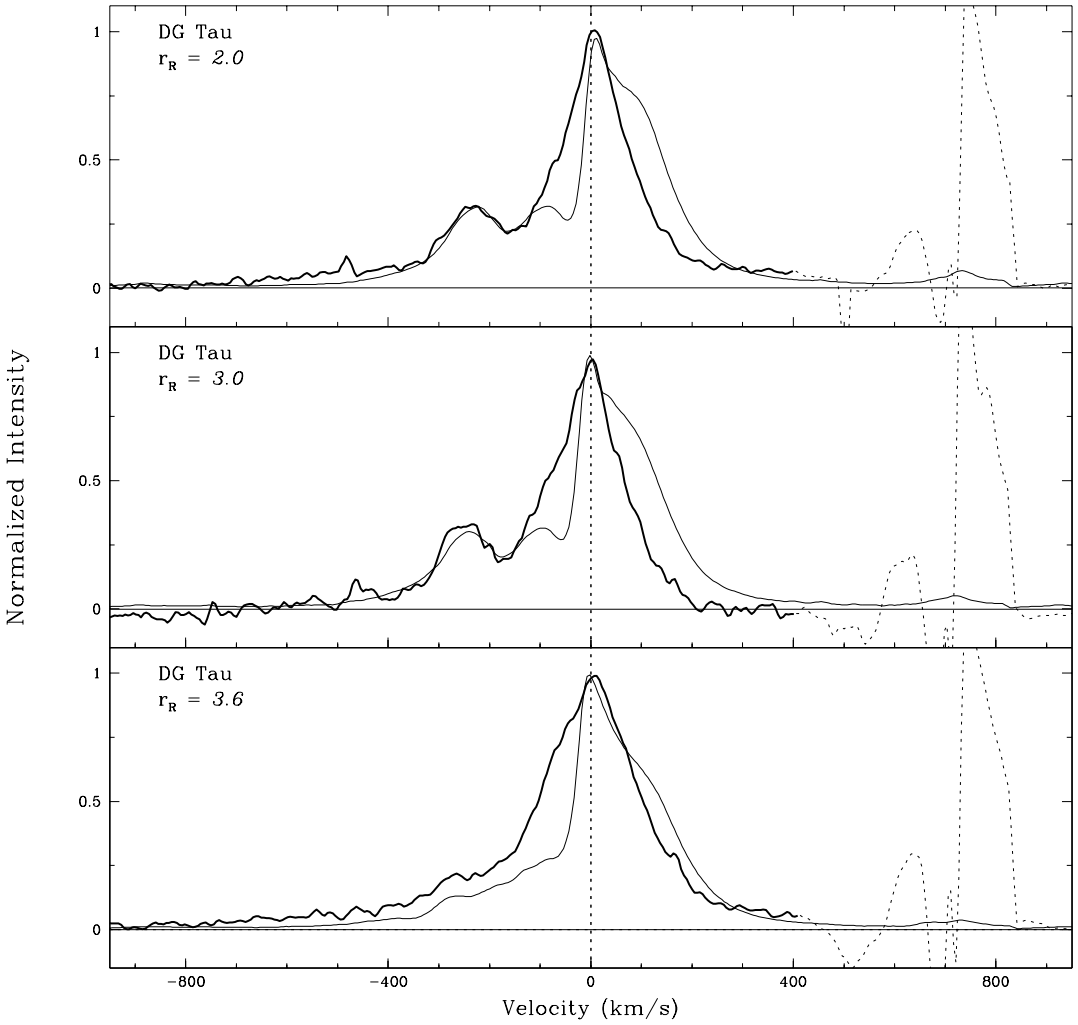

FIG. 8.—Simultaneous He I λ5876 (*thick line*) and Hα (*thin line*) profiles are displayed for all three observational epochs for DG Tau, the only star where we find evidence for blueshifted helium absorption and where blue helium wings extend beyond -500 km s^{-1}. The two lines show remarkably similar structure blueward of -175 km s^{-1}. The velocity range is almost twice that in the other figures, and all profiles are normalized to the line peak. The feature 500 km s^{-1} redward of He I, shown as a dotted line, is the blue wing of the neighboring Na D2 line.

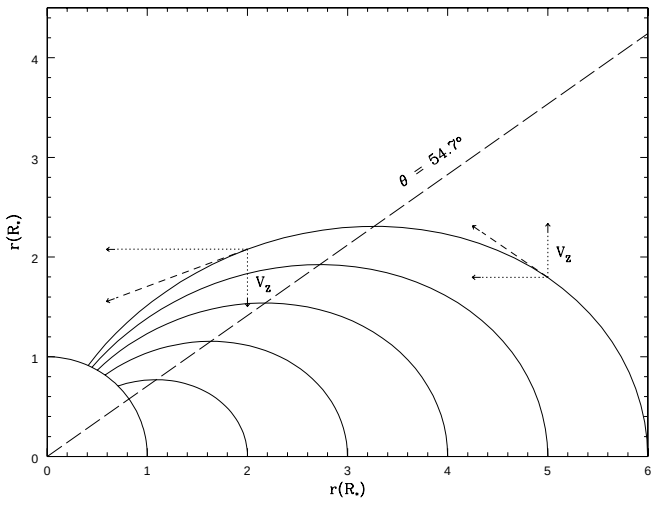

FIG. 9.—Sketch showing the behavior of v_z, the component of the poloidal velocity perpendicular to the disk plane, at different polar angles in an idealized funnel flow. At a polar angle $\theta = 54.^\circ7$, v_z changes sign on all dipole field lines. See § 6 for a discussion of the relevance of v_z to the observed centroid velocity of an optically thin line formed in a magnetospheric funnel flow.

the inclination angle of the line of sight from the z-axis (Kwan & Tademaru 1995). The centroid velocity of the total emergent profile from all infalling material above the disk plane, assuming optically thin emission and no occultation from the star, will then be determined by the $-v_z \cos i$ from the full sequence of rings. It will thus be strongly influenced by the range of polar angles in the funnel flow contributing to the line emission. In particular, the relative contribution of emitting gas inside and outside the critical polar angle $\theta = 54.^\circ7$ determines whether the profile has a redshifted or blueshifted centroid. It is instructive to examine each of the following two cases.

1. If emission predominately arises from polar angles $\theta < 54.^\circ7$, the centroid velocity will be redshifted. Over this range of small polar angles $-v_z$ will span from 70 to 0 km s^{-1} (for $M_* = 0.5\ M_\odot$, $R_* = 2\ R_\odot$, and an inner disk radius of $2R_*$). Thus, emission contributed by material from above the disk plane will be redshifted in the absence of occultation. The effects of occultation on emission at small polar angles above the plane will only be important at large inclinations, when occultation of the approaching gas will

reduce the emission on the blue side, thereby enhancing the redshift of the profile obtained ignoring occultation. The emission from corresponding material below the disk plane ($\theta = \pi - 54.^\circ7$ to $\theta = \pi - \theta_0$) would be a blueshifted reflection of that from above the plane if there were no occultation by the star. Here, however, occultation is severe and present at all viewing angles, and the star again preferentially eclipses blueshifted emission. Thus, the summed profile from both hemispheres remains redshifted.

2. A blueshifted emission centroid will result if there is a significant contribution to the emission from polar angles $\theta > 54.^\circ7$. At these large polar angles $-v_z$ ranges from -45 to 0 km s^{-1} for the stellar values given above, with the most negative velocity coming from a narrow ring around $\theta \sim 70^\circ$. For example, if there is an equal contribution to the emission from each unit volume in the funnel flow, the much larger volume of material at $\theta > 54.^\circ7$ will produce a blueshifted profile. For no stellar occultation, the material above the disk plane could produce a centroid velocity blueshifted by as much as -30 km s^{-1} if it were viewed at the most favorable inclination angle, $i = 0^\circ$, but it would be reduced to -15 km s^{-1} for an average value of cos i. The effects of stellar occultation above the disk plane depend on the inner edge of the disk and the viewing angle. The most significant effect will be for large inclinations, where occultation by the star reduces the blueshift of the centroid. For emission below the plane, occultation by the disk of material at large polar angles is so severe that this emission makes a minimal contribution to the summed profile from both hemispheres.

In addition to the line centroid, we can also set constraints on the velocities of the emission wings for profiles arising in funnel flows:

The maximum blue wing velocity that will be produced in infalling magnetospheric gas will be less blueshifted than -200 km s^{-1}. The maximum velocity achieved in a nonrotating funnel flow is the poloidal velocity as the material is just approaching the stellar surface. For inner disk radii ranging from $2R_*$ to $6R_*$ (θ_0 from 45° to 24°) these values will be between 220 and 280 km s^{-1} for $M_* = 0.5\ M_\odot$ and $R_* = 2\ R_\odot$. If the emission from above the disk plane is viewed from a typical inclination of $i = 60^\circ$, this maximum poloidal velocity will be foreshortened, possessing a line-of-sight velocity $v_{\rm los} = -v_z \cos i \pm (v_p^2 - v_z^2)^{1/2} \sin i$, where the sign in front of the square root is positive for the red wing, arising from infalling gas directed away from the observer, and negative for the blue wing, arising from infalling gas approaching the observer. For the stellar and disk parameters given above, the maximum red wing velocities will be between 215 and 260 km s^{-1} while the maximum blue wing velocities range from only -85 to -145 km s^{-1}. The focus is not on the observed ratio of redward to blueward emission, which can be affected by occultation and redshifted absorption, but on the upper limit to the blue wing velocity. Although the precise values for the maximum blue wing emission will depend on stellar parameters and inclination, we do not think that magnetospheric infall can consistently account for blue wing velocities in excess of -200 km s^{-1}.

These simple constraints on the centroid velocity and blue wing velocity for profiles formed in optically thin magnetospheric gas have important implications for the origin of the helium emission. Owing to the high-excitation potentials of the helium lines, helium emission is almost certain to arise from recombination and cascade following ionization. In the magnetospheric accretion model the ionizing flux is most likely generated in the accretion shock at the stellar surface. This radiation would preferentially ionize infalling material at small polar angles. In this case helium emission would arise primarily at polar angles with $\theta < 54.^\circ7$, and the constraint on centroid velocity discussed above implies that a redshifted profile would result. Observationally, we find helium BCs with centroid velocities redshifted in excess of 8 km s^{-1} in seven stars in at least one observing epoch (five from the reference sample: DD Tau, DF Tau, DO Tau, DS Tau, and YY Ori; and two from other epochs: DQ Tau and UY Aur). This leads us to propose that in these stars the redshifted BC helium emission arises in the magnetospheric funnel flow from material primarily at $\theta_0 < \theta < 54.^\circ7$ and $\pi - 54.^\circ7 < \theta < \pi - \theta_0$.

The second implication is that magnetospheric gas cannot be the source of the helium BC emission for those profiles with centroids blueward of -30 km s^{-1}. Blueshifted centroids exceeding this value are seen in BC emission from seven stars in at least one observing epoch (all are in the reference sample: AS353 A, CW Tau, DQ Tau, DR Tau, GK Tau, RW Aur, and UY Aur). The third implication is that magnetospheric gas cannot account for the majority of the observed blue wing velocities where 14/22 stars have extreme blue wing velocities that exceed -200 km s^{-1} and 11/22 exceed -300 km s^{-1} in the reference sample.

The combination of the above arguments leads us to the further conclusion that it is unlikely that the BC helium profiles with modest blueshifts and blue wing velocities in excess of -200 km s^{-1} have a significant contribution to their emission from a funnel flow. Given the constraint that helium probably requires proximity to ionizing radiation, generating stronger emission from $\theta > 54.^\circ7$ in order to produce a blueshifted centroid is problematic. Moreover, since magnetospheric emission restricted to small polar angles provides the best explanation for the redshifted BC centroids in about one-fourth of the sample, it would follow that significant emission from large polar angles in the rest of the sample would be unlikely. As will be shown in § 7, compared to objects with blueshifted BC centroids, those with redshifted ones have comparably high veiling levels and stronger NC emission, so there is no reason to expect that these two groups would have large differences in their ionizing flux levels.

These arguments point toward a second source of helium emission, and we suggest that outflowing gas that suffers occultation of receding material by the star and disk is necessary to account for blueshifted centroids and blue wing velocities in BC helium profiles. We refer to it as a hot wind on account of its ability to excite helium, and we infer it to be significant in at least 15/22 stars with BC helium emission in the reference sample. These 15 stars either possess BC centroids blueshifted in excess of -30 km s^{-1} or have modest centroid blueshifts coupled with blue wing velocities in excess of -200 km s^{-1}. This represents 68% of the objects with BC helium emission and 48% of the full sample of objects.

Our arguments in favor of a contribution from a hot wind are not in contradiction with the radiative transfer models developed by Hartmann and collaborators for hydrogen (HHC94; Muzerolle, Calvet, & Hartmann 1997,

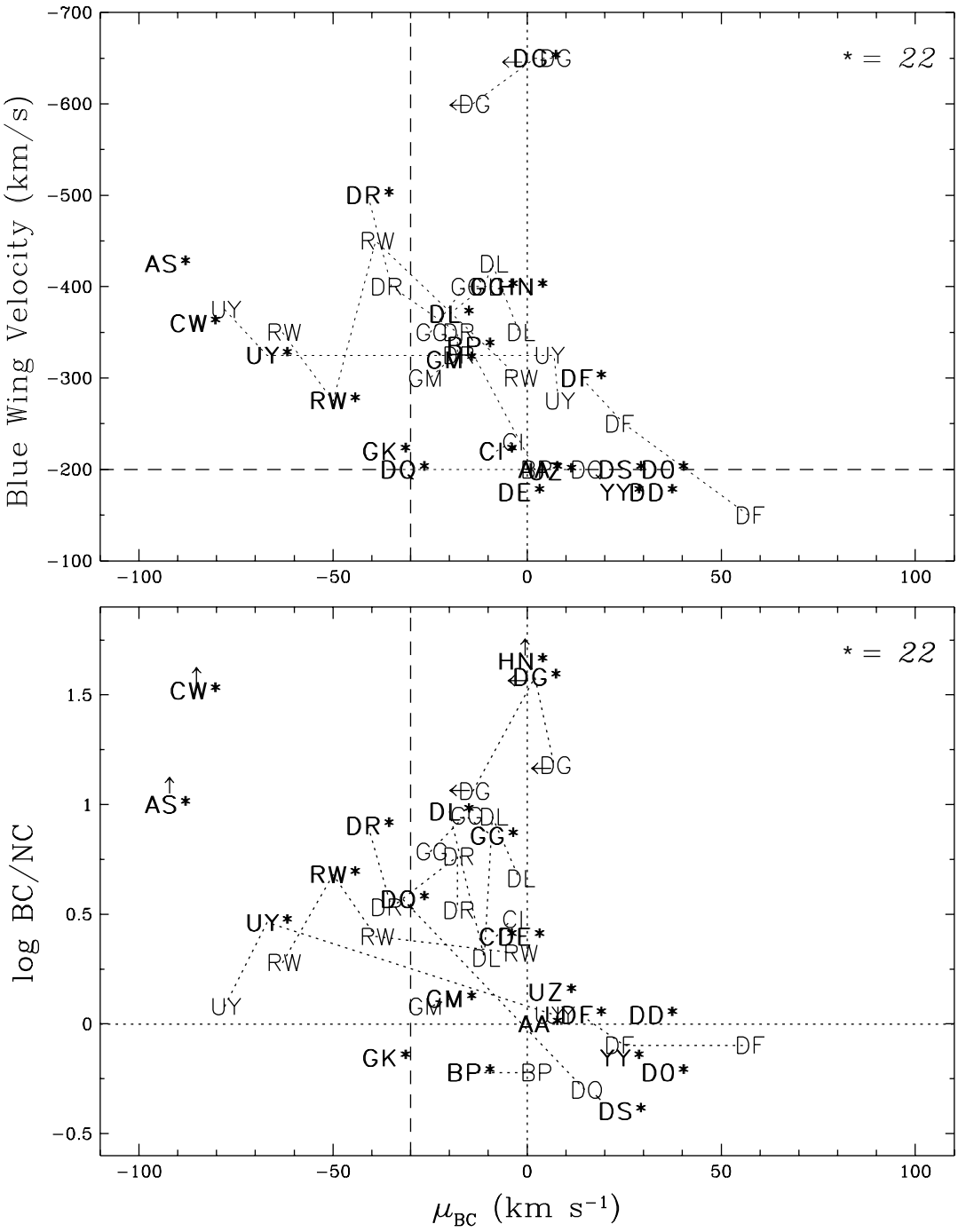

FIG. 10.—Behavior of the He I λ5876 BC centroid velocity, μ_{BC}, in relation to both the BC blue wing velocity (*upper panel*) and the fraction of the helium emission contributed by the BC, BC/NC (*lower panel*). All observational epochs of the 22 stars from the reference sample with BC emission are displayed, with reference sample data shown by an asterisk. Those objects with redshifted BC emission, which we attribute to formation at small polar angles in a funnel flow, are seen to have the lowest blue wing velocities and the smallest contribution of BC emission to their total profile. In contrast, those with blueshifted BC emission, which we attribute to formation in a hot wind, have the largest blue wing velocities, and their helium emission is dominated by the BC.

2001). They assume that hydrogen emission arises fairly uniformly along the full length of the accretion column, in contrast to our suggestion that helium emission arises from small polar angles in the funnel flow. Under their assumption, modest blueshifts in the profiles are predicted, and indeed this has been used as supporting evidence for the prevalence of magnetospheres in classical T Tauri stars (HHC94; Edwards et al. 1994). Although radiative transfer effects, dependent on opacity, excitation, rotation, etc., will affect the shape and peak of the profile, they will not significantly shift the centroid of the emission. Inspection of the published model profiles supports this conclusion, in that none of them have centroid blueshifts in excess of -30 km s^{-1}. The expectation that blue wing velocities in excess of -200 km s^{-1} are not characteristic of magnetospheric emission is also borne out by the model profiles. Although extended wing emission will be generated if line damping effects are important, as recently calculated for Hα by Muzerolle et al. (2001), this effect is not likely to be prominent for helium lines because their opacities are expected to

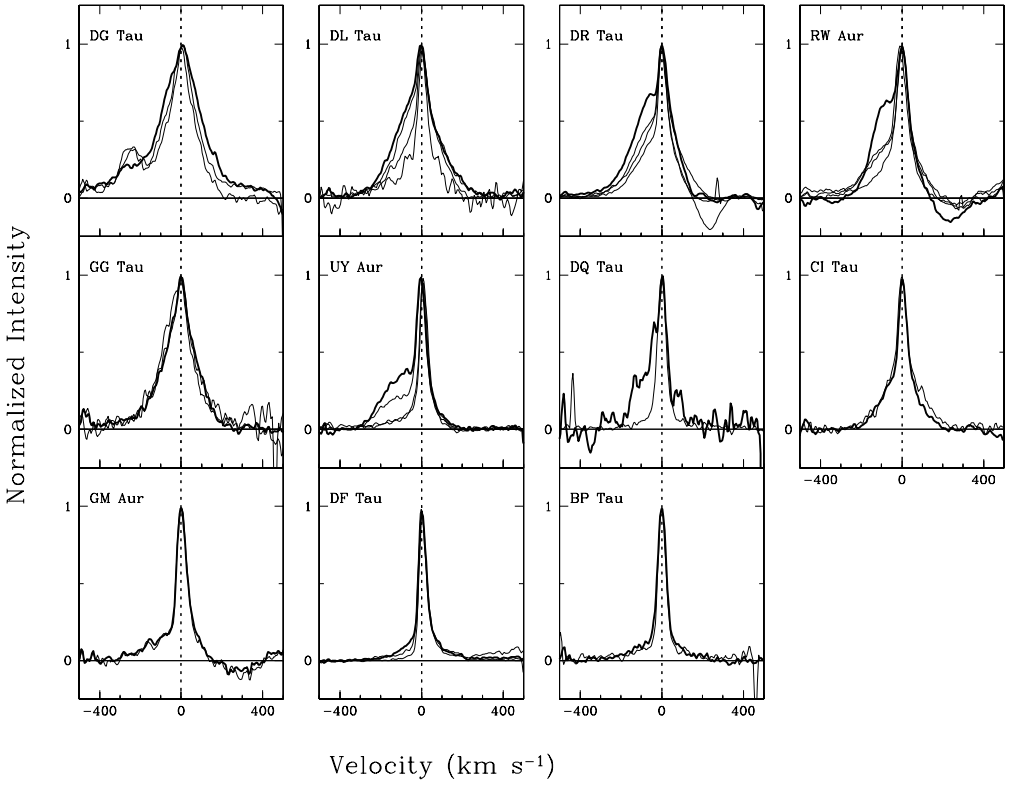

Fig. 11*a*

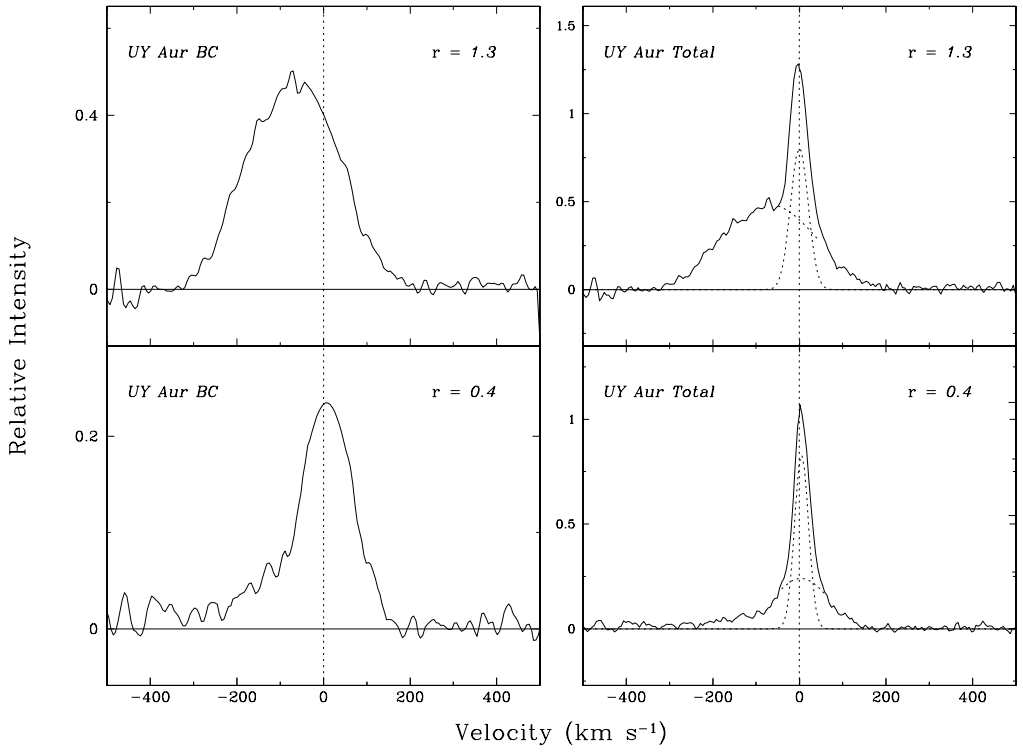

Fig. 11*b*

FIG. 11.—(*a*) Temporal changes in the He I λ5876 profile for those 11 stars with BC emission and multiple observations. The boldface profile is from the reference sample, and all profiles are normalized to their peak values. The BC morphology is variable in about half of the stars with multiple observations, with the blue and red sides varying independently of each other. (*b*) Temporal changes in the He I λ5876 profile for two epochs of UY Aur illustrating the BC centroid shifting from blue to redshifted emission. The upper panel shows an epoch with a blueshifted centroid ($\mu_{BC} = -67$ km s^{-1}, $r = 1.3$, and the BC equivalent width is 2.5 Å), for both the residual BC (*upper left*) and the total profile (*upper right*). The lower panel shows an epoch with a redshifted centroid ($\mu_{BC} = 8$ km s^{-1}, $r = 0.4$, and the BC equivalent width is 0.8 Å), again with the residual BC (*lower left*) and the total profile (*lower right*). The NC equivalent width is comparable in both epochs, but when the BC is wind-dominated, BC/NC is increased by a factor of 3.

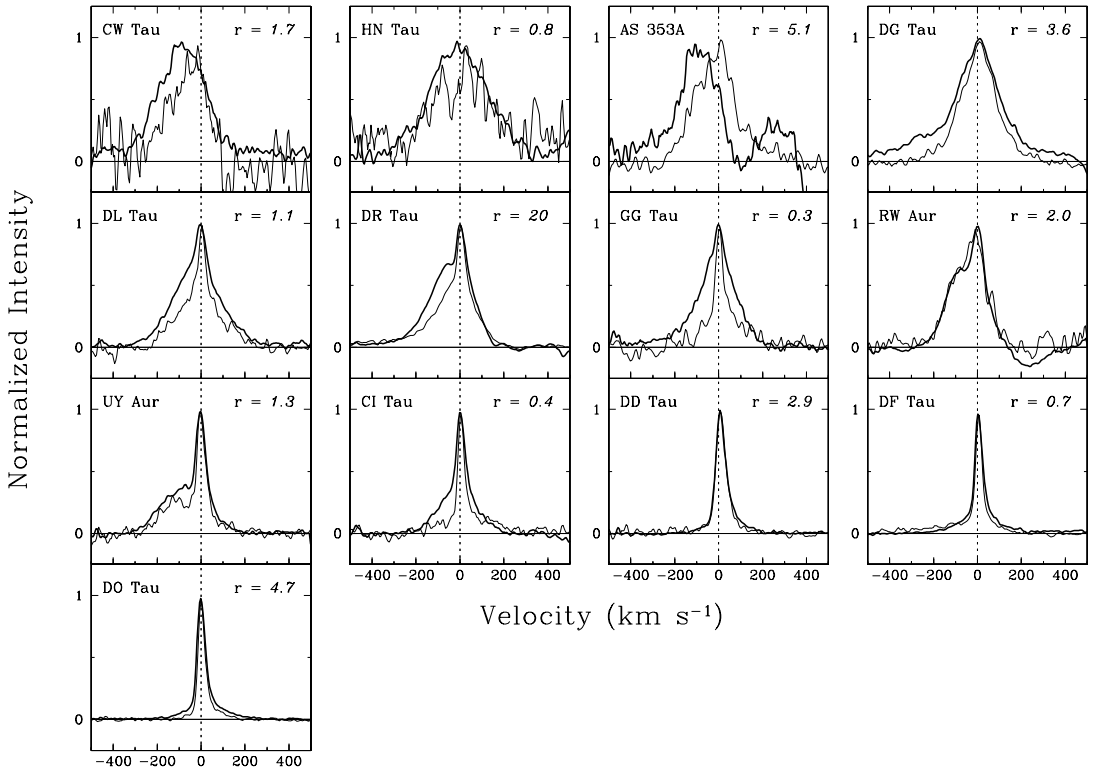

FIG. 12.—Comparison of simultaneous He I λ5876 (triplet) and He I λ6678 (singlet) profiles for 13 stars from the reference sample. The triplet-to-singlet ratio is comparable for the NC of all stars (see Fig. 4). The ratio is larger for the BC and furthermore is larger on the blue compared to the red side of the BC. All profiles are normalized to the line peak.

be much smaller than the hydrogen line opacities. Except possibly for DG Tau, the helium profiles shown in Figures 1*a* and 7 do not appear to have a significant underlying damping wing component, both in terms of the narrower velocity extent than Hα (see Fig. 15) and the significant asymmetry between the red and blue wings.

If the inference of a hot helium wind is correct, we might expect to find correlated behavior between kinematic properties of the BC and other profile characteristics. In Figure 10 we show that the λ5876 BC centroid velocity is sensitive to both (1) the extreme blue wing velocity and (2) the fraction of the emission contributed by the BC to the total profile, evaluated by the equivalent width ratio of BC/NC (Table 2). All observed epochs are included in the figure, with multiple observations of the same star connected by dotted lines. The figure reveals that when the BC is redshifted, and likely accretion dominated, blue wing velocities are always less extended than -300 km s^{-1}. For these stars the bulk of the helium emission is contributed by NC emission, with BC/NC ≤ 1, implying that when the hot wind is weak or absent the dominant source of helium emission is from the NC. In contrast, when the BC is blueshifted, and likely wind dominated, the majority of the blue wing velocities exceed -300 km s^{-1}. For these objects the BC emission dwarfs the NC contribution to the profile, with BC/NC ≥ 1, implying that when the hot wind is present it is often the dominant source of helium emission. This further implies that it is easier to excite helium in the wind than in the funnel flow.

Additional evidence that the BC helium emission is composite comes from (1) comparing time variations in λ5876 profiles and (2) comparing triplet to singlet (λ5876/λ6678) profiles. In Figure 11*a* we superpose normalized λ5876 profiles (NC + BC) for the 11 classical T Tauri stars with BC emission and multiple observations. Half of the stars undergo significant variations in their BC profile morphology, and most of this variation occurs on the blue side of the BC profile, suggesting not only that helium emission from the wind and funnel flow vary independently but also that greater fluctuations occur in the outflowing gas. Two stars, DQ Tau and UY Aur, transition from objects where $\mu_{BC} < -30$ km s^{-1} to $\mu_{BC} > 8$ km s^{-1}. We demonstrate this transition from a wind-dominated to an accretion-dominated BC in UY Aur in Figure 11*b*. In total we have five observational epochs of UY Aur, four of which show BC emission. For two of these epochs, μ_{BC} is blueshifted by about -70 km s^{-1}, and in the other two μ_{BC} is redshifted by about 8 km s^{-1}, while the FWHM of the BC drops from 250 to 150 km s^{-1}.

In Figure 12 we superpose normalized λ5876 and λ6678 profiles (NC + BC) for the 13 classical T Tauri stars with BC emission in both lines. Recalling that the triplet-to-singlet ratios for the NC are fairly uniform (Fig. 5), the normalized profiles in Figure 12 allow a visual comparison of the behavior of the triplet-to-singlet ratio for the BC. It can be seen that the most common distinction is a larger triplet-to-singlet BC emission ratio on the blue rather than on the red side of the profile. This is consistent with the finding in § 3 and Figure 5, where we found larger triplet-to-singlet ratios for the BC emission than the NC emission.

7. FUNNEL FLOWS, ACCRETION SHOCKS, AND HOT WINDS

In the previous section we argued that the He I BC emission is itself composite, arising partly in the funnel flow and partly in outflowing gas. The possibility that the total

helium emission has contributions from three regions (a funnel flow, an accretion shock [NC], and a wind, each of which must be either in a region of very high temperature or close to a strong source of ionizing radiation) motivates us to investigate further the relation between these components. Within the paradigm that classical T Tauri stars are low-mass stars with active accretion disks and accretion-driven outflows, we would expect these three components to be correlated with each other and with the continuum veiling, which is the basis for the empirical calibration of the mass accretion rate. Certainly such trends are seen between forbidden line luminosity and the veiling-derived mass accretion rate (HEG95; Gullbring et al. 1998), indicating that the energy budget for classical T Tauri stars appears to be controlled by the disk accretion rate. In this section we examine the relations between the various helium components and the simultaneously derived continuum veiling, which is believed to occur in the postshock gas (Calvet & Gullbring 1998).

As discussed in the previous section, when conditions favor the generation of a hot wind, it generally becomes the dominant source of BC emission in the He I profile. However, when both wind and accretion contribute to a composite BC profile, it is difficult to disentangle the separate contributions of these two sources. As a gauge of the strength of helium emission in accreting funnel flow gas, we use the BC equivalent width for seven stars with redshifted BC emission. As a gauge of the strength of the wind contribution, we use the BC equivalent width for seven stars with BC emission blueshifted by more than -30 km s^{-1} plus DG Tau, which shows blueshifted absorption at λ5876. The relation between each of these two diagnostics with the simultaneous NC and veiling emission is illustrated in Figure 13. As in the previous figures, the equivalent widths are corrected for veiling in order to make them proportional to line flux. We find distinctly different behaviors depending on whether the sources are accretion- or hot wind–dominated. For the stars identified with accretion-dominated BC emission, there is a correspondence with both the veiling and the NC flux, as would be expected if the line and the continuum emission from the postshock gas correlate with the line emission from small polar angles in the funnel flow. In contrast, for the stars with wind-dominated BC emission, the BC line flux correlates with the veiling but not with the NC flux.

The relations shown in Figure 13, although based on only a subset of our sample, suggest that the BC helium emission correlates with the NC emission only when the hot wind is weak or absent. The implication seems to be that when the hot wind becomes strong, the characteristics of the accretion shock, as traced by the NC, are altered. In order to test this hypothesis, we recall the relation between NC emission and veiling for the full sample of 31 stars examined in § 3. In the classical picture where both veiling and the NC should arise in the accretion shock, they would be expected to correlate. Instead, we found little correspondence between

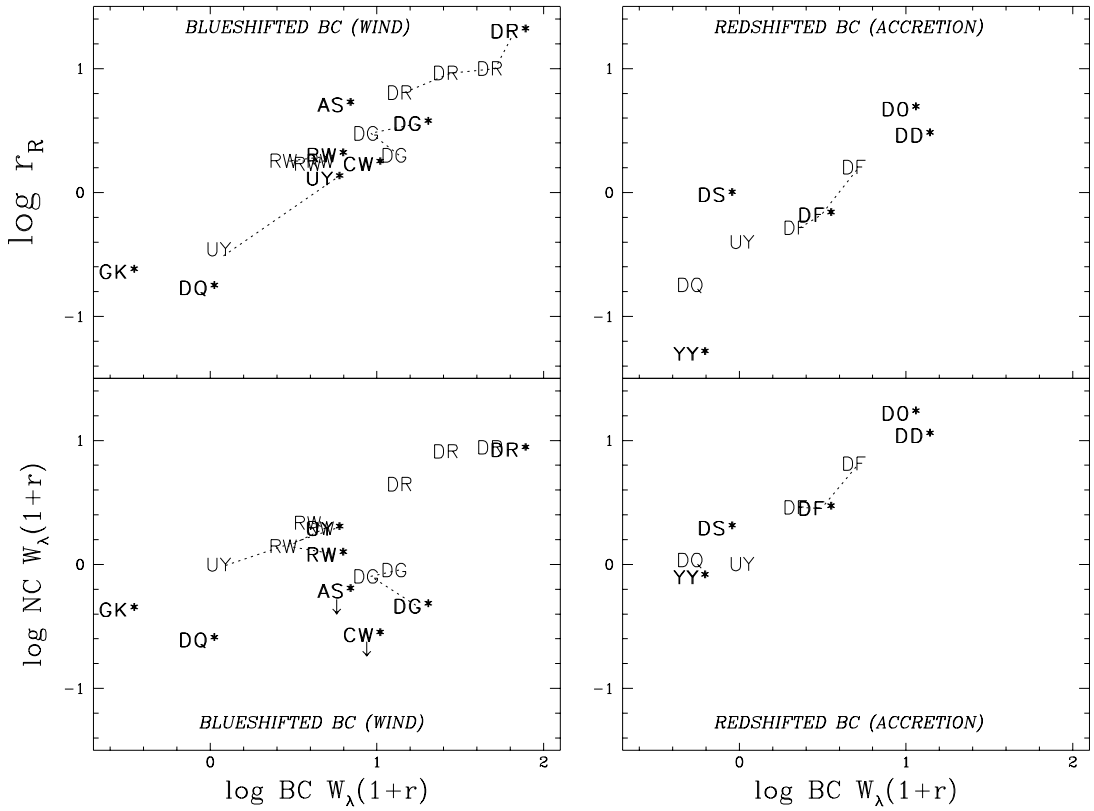

FIG. 13.—Comparison of the relation between BC He I λ5876 emission and both NC emission and veiling for two subsets of our sample, comprising a total of 14 of the 22 stars with BC emission. In the left panel are (multiple) observations of eight stars with the strongest evidence for a hot wind: either $\mu_{BC} < -30$ km s^{-1} or a blueshifted absorption at λ5876. In the right panel are (multiple) observations of seven stars where the BC is likely accretion dominated, with μ_{BC} redshifted by ≥ 8 km s^{-1} (one star, UY Aur, appears in each group at different observational epochs). The relation between NC and BC line flux [traced by $W_\lambda(1 + r)$] differs for the wind- and accretion-dominated groups, although both have similar correlations between BC emission and veiling.

them for the full data set of 31 classical T Tauri stars, as shown earlier in Figure 4. Guided by the different behavior of the NC between stars with redshifted BC centroids and those with extreme blueshifted BC centroids, we reexamine the relation between NC emission and veiling for our full data set by separating it into two groups: stars with or without an indication of a hot wind. The group with no evidence for a hot wind is comprised of 16 stars (nine with NC-only emission plus seven with redshifted BC emission). As seen in the upper panel of Figure 14, for these 16 stars with no evidence for a hot wind there is a good relation between the NC and veiling, suggesting a close connection between them, presumably through the accretion shock.

The second group for which we compare NC emission and veiling is comprised of 17 stars with BC emission that is not redshifted, shown in the lower panel of Figure 14. (The total from the two groups is 33 stars because two stars fall into both groups at different epochs). Comparison of the upper and lower panels of Figure 14 reveals that there is a different relation between NC emission and veiling for stars

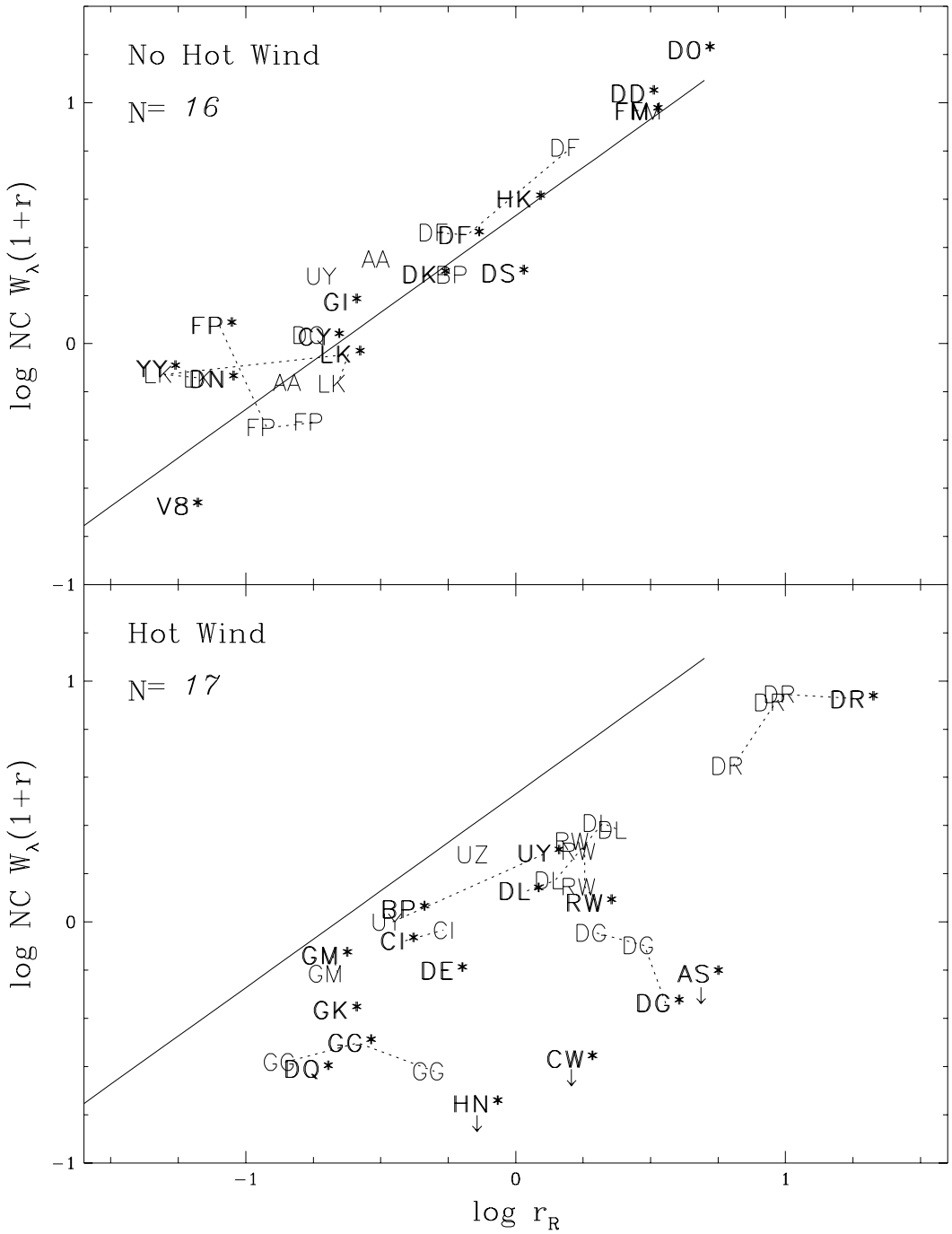

FIG. 14.—Comparison between the NC line flux and the veiling for two subsets of stars, comprising all 66 observations of our complete sample of 31 classical T Tauri stars. In the upper panel are the 17 stars with no evidence for a hot wind (either NC-only or redshifted BC emission). In the lower panel are the 16 stars that appear to have a hot helium wind (BC is present but not redshifted). In both panels the best-fit line to the NC vs. veiling for the stars with no hot wind (*upper panel*) is shown. The relation between NC emission, formed in postshock gas, and the veiling is distinctly different for the objects with and without a hot helium wind.

with and without hot winds. For many of the stars with hot winds a correspondence between NC emission and veiling appears to be present, but the NC emission is weaker at a given veiling level in stars with hot winds than in stars that lack them. Moreover, there are five objects with hot winds where the NC emission is anomalously weak for the observed veiling, and three of these have no detectable NC λ5876 emission at all ($W_\lambda < 0.1$ Å; AS 353A, CW Tau, and HN Tau). The absence of NC emission in these three stars applies through the full spectral range of our red and blue orders. Among low-excitation lines of Fe I, Fe II, Ti II, and Mg I, the profiles are also BC only. Furthermore, these are the only three stars where we do not observe any He II λ4686 emission, which is present as an NC-only profile in all other stars with blue spectra. We interpret the relations in Figures 13 and 14 as evidence that the NC emission is reduced relative to the veiling, sometimes to the point of extinction, in stars that possess hot helium winds. These differing behaviors account for the confused relation between NC emission and veiling for the combined data set shown in Figure 4 and found by other authors.

We offer a possible scenario for the differing relation between NC emission and veiling in stars with or without a hot wind. We note that the hot wind is usually coexistent with magnetospheric accretion, so if it comes from the star it is likely to be from the polar regions, where coronal winds will have the temperature to accelerate the gas and excite helium.

When the hot wind is weak or absent, the funnel flow and accretion shock seem to behave as expected within the classical paradigm, where the veiling, NC, and BC are all correlated. The veiling in these stars would arise in the shocked gas at the magnetosphere footpoint, as suggested by previous investigators (Bertout 1989). Those objects with the lowest accretion rates (lowest veiling) probably do not have sufficient ionizing radiation from the shock to photoionize helium in the magnetospheric columns, and the line is seen as NC only. Observationally, we find that of the nine stars with NC-only λ5876 profiles, only two have $r_R \geq 1$, while six have $r_R \leq 0.2$. In contrast, for those stars with redshifted BC emission, three of seven stars have $r_R \geq 1$ and only two have $r_R \leq 0.2$, indicating that these stars have higher veiling on average than the NC-only group. This is consistent with a picture where an increase in the disk accretion rate results in increased luminosity in the accretion shock with a corresponding increase in the production of ionizing radiation that enhances redshifted BC emission from helium via interception of the radiation at small polar angles in the funnel flow.

However, among the stars with higher veiling, onset of the hot wind can occur and the NC emission no longer correlates with the BC emission or the veiling. In our data set, BC emission blueshifted in excess of -30 km s^{-1} is more likely to be found in stars with $r_R > 1$ (five of seven stars), levels comparable to those found for the redshifted BC objects. Although it is conceivable that reduction in the NC emission in these objects can be attributed to occultation of the shock (Hamman & Persson 1992), we are intrigued by the possibility that the funnel flow and accretion shock may be altered in those stars with strong helium winds. High accretion rates or weak stellar fields could lead to the magnetosphere being crushed sufficiently that the disk extends almost to the star so stellar field lines interrupting the disk will originate from the star at a low latitude. Infall velocities will be smaller, leading to lower postshock temperatures and reduced NC helium emission. At the same time, the polar region of the star, from which a hot wind may emerge along open field lines, would be more extensive. The existence of a polar/coronal wind in classical T Tauri stars has also been suggested by Camenzind (1997) and Shu et al. (1994). Our data indicate that a polar wind may actually be quite prevalent, although it is strongest in stars with higher than average accretion rates and absent in stars with the lowest accretion rates, indicating that it is initiated by phenomena related to accretion.

The fact that optical veiling correlates with BC emission whether or not NC emission from an accretion shock is visible suggests that there may be two sources of optical veiling operating in disk-accreting classical T Tauri stars. In the stars lacking hot winds the veiling would arise in the postshock gas at the base of the funnel flow. In those stars with hot winds the veiling appears to arise elsewhere, although it is unlikely that it comes from the hot gas in the polar region where the wind is hypothesized to emerge. In contrast to the magnetospheric footpoints, the filling factor of the hot wind would be considerable, and it would be impossible to reconcile the observed veiling spectrum and inferred optical depth with an origin over a large fraction of the star. However, in the scenario we posit for the hot wind to arise, one might expect to generate optical continuum emission at the disk/magnetosphere interface in stars with crushed magnetospheres rather than at the star/magnetosphere boundary. In contrast to the classical picture, considerable rotational energy would have to be dissipated by accreting material in the case of small disk truncation radii and short magnetospheric loops before it could accrete onto the star. If this energy is dissipated thermally, the observed optical veiling in stars with hot winds but no apparent accretion shocks could thus be accounted for.

To round out the speculative scenario we offer here, we note that if there is an extended polar region with both closed coronal loops and open field lines from which hot winds escape the star, a significant Lyman continuum excess from this region would also be expected, providing an explanation for the observation that it is easier to excite helium in the wind than in the accretion flow. Although this continuum excess would not be observed in optical veiling, we predict that stars with hot winds will be characterized by higher levels of Lyman continuum excess than stars that lack these hot winds.

8. RELATION TO OTHER WIND DIAGNOSTICS

Analysis of the BC emission from helium has led us to conclude that a hot wind must originate close to the stellar surface in classical T Tauri stars with high disk accretion rates. Onset of this hot wind, which we suggest emerges from coronal regions, does not preclude the presence of a disk wind. The fact that both may be present is in fact inferred from comparing observational diagnostics of the hot wind to those for the inner wind traced by blueshifted absorption in strong permitted lines and for the outer collimated wind traced by blueshifted emission in forbidden lines. In this section we make this comparison for Hα and [O I] λ6300 profiles that are observed simultaneously with He I λ5876.

In Figure 15 we present the Hα profiles observed simultaneously with the 31 reference sample He I profiles that were

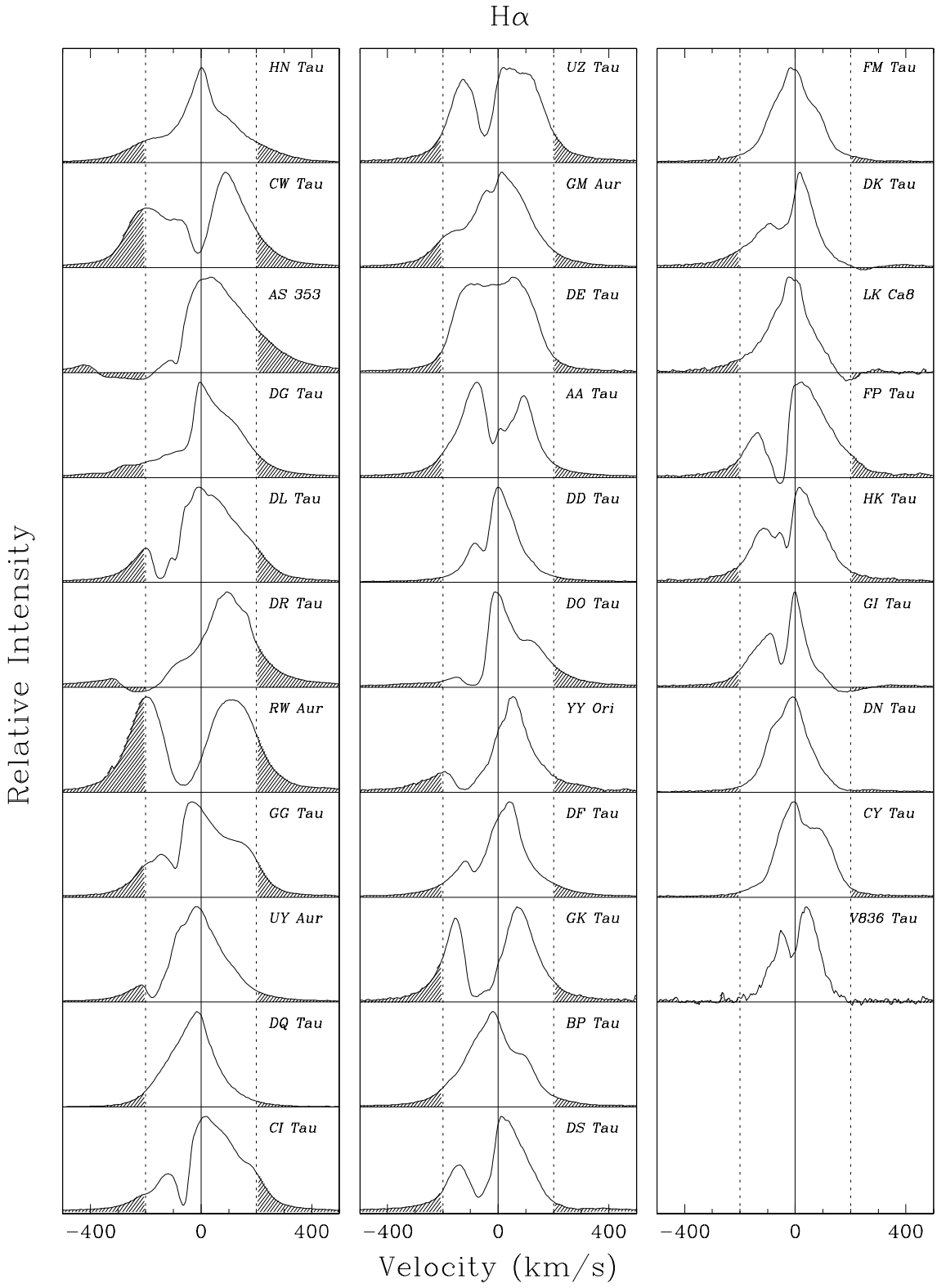

FIG. 15.—Hα profiles observed simultaneously with λ5876 for all 31 classical T Tauri stars in the reference sample, arranged in the same order as Fig. 1. The emission outside of ±200 km s^{-1} is shaded in order to assess visually the wing asymmetry. The presence of blueshifted P Cygni absorption below the continuum level in two stars (AS 353A and DR Tau) and redshifted inverse P Cygni absorption below the continuum level in three stars (DK Tau, LK Ca 8, and GI Tau) acts to invert the sense of their wing emission asymmetry.

shown in Figures 1*a* and 1*b*. We first focus on the wings of the Hα profile and argue that some of the wing emission likely arises in the hot coronal wind. The large line width and overall baseline symmetry of Hα in classical T Tauri stars were pointed out two decades ago (Decampli 1981). Most recently, this line was modeled as arising primarily in the funnel flow, with the large wing velocities attributed to Stark broadening (Muzerolle et al. 2001). If Hα arises pri-

marily in a funnel flow, there should be a modest redward asymmetry in the wing emission due to occultation by the star of material infalling at a terminal velocity that is approaching the observer (redshifted absorption could reverse this to a blueward asymmetry, but it is rare at Hα, and then only in stars with the lowest veiling). On the other hand, if contribution from a wind is important, the wing emission will reflect a blueward asymmetry as a result of occultation of the receding flow by the star and disk. Our spectra are of sufficient quality to test the symmetry in the line wings, where we focus on emission at velocities exceeding ± 200 km s^{-1}. Equivalent width measurements for the blue and red wings, along with the total equivalent width and a wing asymmetry index for Hα, are listed in Table 5 for all observations of our 31 classical T Tauri star sample. We define the wing asymmetry index as $(R - B)/(R + B)$, where R and B are the red and blue equivalent widths measured beyond ± 200 km s^{-1} in the Hα profile. This index effectively subtracts any contribution from Stark wings, which are expected to be symmetric.

In Figure 16 we present a histogram of the Hα wing asymmetry index for the reference sample profiles shown in Figure 15, excluding V836 Tau since its B, R equivalent widths are less than 0.1 Å and a meaningful index cannot be calculated. The histogram shows that one-third of the objects (10/30 stars) have symmetric wings at Hα, with $|(R - B)/(R + B)| < 0.1$. There are five stars with wing asymmetry indices $|(R - B)/(R + B)| > 0.4$. In all five the presence of either blueshifted P Cygni absorption below the continuum level (AS 353A and DR Tau) or redshifted inverse P Cygni absorption below the continuum level (DK Tau, GI Tau, and Lk Ca8) shifts the index to extreme redward or blueward values, respectively, in opposition to the sign that would characterize the index of the underlying emission profile. Turning our attention to the remaining 15 stars, we find that blueward wing asymmetries are seen in 11 objects, with $(R - B)/(R + B)$ between -0.1 to -0.4, while only four have redward asymmetries, with $(R - B)/(R + B)$ between 0.1 to 0.4.

The prevalence of blueward over redward asymmetries in Hα in profiles whose wings beyond 200 km s^{-1} are not skewed by redshifted or blueshifted absorption features suggests that there is a contribution to Hα emission from outflowing gas. This conclusion is strengthened by that fact that out of the 11 profiles with blueward wing asymmetries at Hα, those five with the larger asymmetry index all have He I λ5876 BC centroids blueshifted by more than -30 km s^{-1}. Inspection of the profiles for these stars (CW Tau, DQ Tau, GK Tau, RW Aur, UY Aur) reveals that the Hα wing emission is distinctly asymmetric to the blue and there is no redward absorption to skew the profile index. The other two stars with helium BC centroids more blueshifted than -30 km s^{-1} (AS 353A and DR Tau) also show evidence for a wind in their Hα profiles; these are the two stars discussed above where P Cygni absorption impinges on the wing emission beyond -200 km s^{-1}, so that their asymmetry index is skewed to the red. In contrast, of the five stars from the reference sample with helium μ_{BC} redward of 8 km s^{-1}, we find that in one star Hα shows a distinctive redward wing asymmetry (DO Tau), two are symmetric (DD Tau, DF Tau), and two (DS Tau, YY Ori) have a small blueward asymmetry.

We note that the wing asymmetry index differs from the asymmetry factor used by Edwards et al. (1994), who quantified the overall asymmetry in Balmer profiles by the ratio of total blueward to total redward emission over the entire profile. In the 1994 paper (which includes about half of the data presented here) the goal was to identify profiles that were significantly affected by blueshifted or redshifted absorption. In the case of Hα, it was found that the total asymmetry factor flipped from redward-dominated emission for stars of high veiling (resulting from blueshifted absorption) to blueward-dominated emission for stars of low veiling, which sometimes show redshifted absorption. The blueward-dominated emission was interpreted as support for magnetospheric accretion, which will produce a modest blueward line asymmetry under the assumption that emission arises over the full length of an accretion column. On the basis of the wing asymmetry index introduced here, we conclude that outflowing gas is a contributor to Hα wing emission in approximately half of our sample, presumably from the same region as the wind traced by BC helium emission.

We next turn our attention to the blueshifted absorption at Hα, which is usually attributed to formation in an inner wind, and compare it to the kinematic properties of the helium profiles. We find that the overall frequency of blueshifted absorption at Hα, seen in 22/31 stars, is the same as that for the occurrence of BC helium emission. However, blueshifted Hα absorption is found in stars both with and without BC helium emission. Among the stars that lack BC helium emission, simultaneous blueshifted absorption at Hα is seen in five of nine stars. Among the stars with BC helium emission, the frequency of blueshifted absorption at Hα is identical in stars with redshifted ($\mu_{BC} > 8$ km s^{-1}) or highly blueshifted ($\mu_{BC} < -30$ km s^{-1}) helium centroids, seen in six of seven stars in each case.

These statistics show that the formation of blueshifted absorption at Hα occurs over a wide range of helium emission properties with no direct connection to the presence of a hot helium wind, although as judged by the comparable flow speeds both must arise within several stellar radii of the central star. The widespread Hα blueshifted absorption could be attributed to the polar/coronal wind we are invoking for helium, which may not be hot enough in some objects to excite helium. However, we consider it more likely that in addition to the hot polar/coronal wind diagnosed by BC helium there is also a cool inner wind, probably a disk wind launched at the magnetosphere/disk boundary as a means of transporting outward the angular momentum of the matter accreting onto the stellar field lines (e.g., Shu et al. 2000). Both of these inner winds could then contribute to blueshifted Hα absorption, and in cases in which the hot wind is weak or absent the blueshifted absorption would come predominantly from the cooler disk wind. This would provide a reasonable explanation for the great variety in the characteristics of the blueshifted absorption features found at Hα, which differ greatly in both their depth and velocity. In some cases these comprise a broad P Cygni structure (e.g., AS 353A, DR Tau, DG Tau—stars with hot helium winds), while in others the feature is sharper, narrower, and occurs at a lower speed (e.g., DD Tau, GI Tau, UZ TauE), which together will be difficult for a single wind acceleration region to produce.

We infer that classical T Tauri star Hα profiles can include emission and absorption contributions from two inner winds. Winds as the major source of Balmer line emission in classical T Tauri stars were rejected a decade ago

TABLE 5

Hα W_λ AND ASYMMETRY INDEX

Object	r_R[a]	W_λ(total)	W_λ(blue)[b]	W_λ(red)[c]	$(R-B)/(R+B)$[d]
AA Tau.....	0.2	8.2 (0.3)	0.9	0.5	−0.32
	0.3	27.8 (0.6)	2.7	2.4	−0.06
	0.6*	76.9 (1.4)	6.8	4.8	−0.17
AS 353A.....	5.1*	54.6 (1.0)	0.2	11.4	0.96
BP Tau.....	0.4*	49.0 (0.4)	4.0	2.9	−0.16
	0.6	39.1 (0.6)	2.6	2.2	−0.07
	0.6	39.6 (0.5)	3.4	2.0	−0.27
CI Tau	0.4*	70.6 (0.9)	6.0	8.7	0.19
	0.5	58.3 (1.4)	6.6	7.2	0.04
CW Tau.....	1.7*	276.5 (5.5)	52.0	29.2	−0.28
CY Tau.....	0.2*	38.9 (0.5)	1.5	2.3	0.21
DD Tau	2.9*	145.1 (2.2)	6.6	7.6	0.07
DE Tau	0.6*	71.2 (0.9)	3.6	3.0	−0.09
DF Tau	0.5	64.8 (0.7)	4.1	4.5	0.05
	0.7*	71.9 (0.7)	5.7	5.9	0.01
	1.6	80.3 (1.2)	4.3	4.5	0.02
DG Tau	2.0	93.1 (4.7)	16.7	10.9	−0.21
	3.0	74.7 (1.9)	14.5	8.5	−0.26
	3.6*	71.2 (2.5)	7.6	7.1	−0.04
DK Tau	0.5*	11.5 (0.3)	1.5	0.4	−0.55
DL Tau	1.1*	121.7 (0.8)	16.2	14.9	−0.04
	1.4	102.9 (1.0)	14.1	14.2	0.00
	2.1	99.6 (0.7)	9.3	11.5	0.10
	2.4	108.2 (0.8)	12.6	13.9	0.05
DN Tau	0.1*	17.8 (0.2)	0.7	0.8	0.03
DO Tau	4.7*	75.6 (1.1)	5.5	10.6	0.32
DQ Tau	0.2*	61.6 (0.4)	4.2	2.1	−0.33
	0.2	61.3 (0.2)	3.0	2.8	−0.02
DR Tau	6.4	88.4 (0.7)	7.4	11.9	0.23
	9.2	56.1 (1.6)	5.5	10.7	0.32
	10	72.6 (2.1)	4.2	15.2	0.57
	20*	70.7 (1.4)	4.7	13.0	0.47
DS Tau.....	1.0*	28.4 (0.9)	3.4	2.4	−0.17
FM Tau	3.0*	74.3 (1.0)	4.1	3.8	−0.04
	3.2	80.6 (1.2)	4.3	4.4	0.01
FP Tau.....	0.1*	24.8 (0.6)	2.2	2.8	0.12
	0.1	40.7 (1.0)	2.1	2.7	0.12
	0.2	18.3 (0.3)	2.1	1.4	−0.19
	0.2	18.3 (0.3)	2.0	1.4	−0.16
GG Tau	0.1	39.4 (0.5)	4.4	3.9	−0.06
	0.3*	45.0 (0.5)	5.1	4.7	−0.05
	0.5	31.5 (0.5)	2.7	2.8	0.02
GI Tau	0.2*	12.8 (0.2)	1.6	0.4	−0.59
GK Tau	0.2*	17.6 (0.5)	2.6	1.6	−0.23
GM Aur.....	0.2*	110.5 (1.4)	10.4	7.1	−0.19
	0.2	110.4 (2.1)	10.5	7.5	−0.17
HK Tau	1.1*	49.5 (0.9)	4.9	4.0	−0.10
HN Tau	0.8*	90.8 (1.5)	12.3	11.0	−0.06
LK Ca8	0.1	2.0 (0.1)	0.2	<0.1	< −1
	0.1	2.5 (0.2)	0.3	<0.1	< −1
	0.2*	7.9 (0.3)	0.8	<0.1	< −1
	0.2	4.0 (0.4)	0.5	0.1	−0.67
RW Aur	1.7	73.4 (1.0)	15.8	13.1	−0.09
	1.8	81.3 (2.0)	16.6	12.6	−0.14
	1.8	59.8 (0.6)	8.4	14.2	0.26
	2.0*	70.0 (1.8)	17.8	9.4	−0.31
UY Aur	0.2	40.3 (0.6)	2.6	2.6	0.00
	0.3	61.4 (0.5)	4.3	3.3	−0.14
	0.4	47.0 (0.5)	3.0	3.0	−0.00
	0.6	56.0 (0.6)	4.8	4.6	−0.02
	1.3*	76.7 (1.1)	8.1	5.1	−0.23
UZ TauE.....	0.7*	70.4 (1.4)	4.9	5.3	0.05

TABLE 5—*Continued*

Object	r_R[a]	W_λ(total)	W_λ(blue)[b]	W_λ(red)[c]	$(R-B)/(R+B)$[d]
V836 Tau.....	0.0	1.4 (0.1)	<0.1	<0.1	...
	0.1*	2.4 (0.2)	<0.1	<0.1	...
	0.1	2.3 (0.1)	<0.1	<0.1	...
YY Ori	0.1*	25.9 (0.8)	3.8	3.0	−0.12

NOTE.—Equivalent widths (in Å) are with respect to the total continuum. Uncertainties are in parentheses.

[a] The veiling at 5200 Å; the reference sample is indicated by an asterisk.

[b] The W_λ for the blue wing of Hα, blueward of -200 km s^{-1}.

[c] The W_λ for the red wing of Hα, redward of 200 km s^{-1}.

[d] The asymmetry index $[W_\lambda(\text{red}) - W_\lambda(\text{blue})]/[W_\lambda(\text{red}) + W_\lambda(\text{blue})]$.

because of their inability to reproduce observed Balmer line profiles in either spherically symmetric or conical geometry (Calvet, Hartmann, & Hewett 1992; but see Mitskevitch, Natta, & Grinin 1993). The assumption that the Balmer lines arise under conditions of collisional excitation required that the lines be very optically thick, leading to the formation of deep blueshifted absorption at large velocities. The failure of these wind models to reproduce the observed line profiles led to the investigation of line formation in magnetospheric funnel flows, where models were better able to reproduce many observed profile characteristics, in particular the centrally peaked emission, slight blueward asymmetries, and occasional redshifted inverse P Cygni absorption found in Balmer lines (Calvet & Hartmann 1992; HHC94). In spite of the success of these models, there remain some discrepancies with observations that have been noted in the literature (Alencar & Basri 2000; MHC98; Folha & Emerson 2001). The analysis presented here suggests that classical T Tauri star emission profiles likely have a composite origin. Each of the published wind or accretion models necessarily relies on a single acceleration region to reproduce the full profile, while the actual situation may be far more complex. The fact that helium emission, which must form under highly restrictive conditions, appears to have three different formation sites suggests that Balmer lines likely have multiple contributions as well. Their blueshifted absorption may arise in one or both of the inner winds, and emission can arise not only from the magnetosphere but also from both winds, the accretion shock, and the magnetosphere/disk boundary. Multiple sites of line formation and temporal variations in their relative contributions could then lead to the broad range in width, centroid, and shape of the Balmer lines. The intensive synoptic studies of Balmer emission in several classical T Tauri stars also suggest multiple origins, where entire line profiles do not vary coherently but instead exhibit different variability behavior in limited velocity intervals (Johns & Basri 1995; Johns-Krull & Basri 1997).

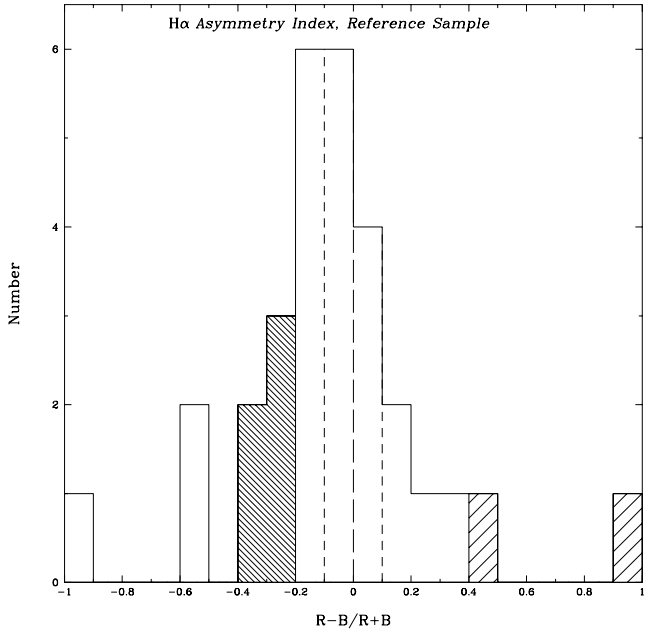

FIG. 16.—Distribution of the Hα wing asymmetry index, $(R-B)/(R+B)$, for red and blue emission beyond ± 200 km s^{-1} for 30/31 stars from the reference sample (V836 Tau has negligible emission at these velocities). The hatching represents the seven stars with the strongest hot-wind signatures. All seven show evidence for a blueward asymmetry in their Hα wing emission, although two of them (AS 353A and DR Tau; *wider spaced hatching*) appear with a large positive asymmetry index because of their Hα P Cygni absorption below the continuum level at velocities in excess of -200 km s^{-1}.

A comparison of the forbidden line profiles with the kinematic properties of the helium lines offers the potential to study the relation between inner and outer winds. The forbidden lines for this data set are presented and analyzed in HEG95. We find that the frequency of blueshifted peaks in [O I] λ6300 is high in stars with BC helium emission, independent of whether they are wind- or accretion-dominated. For example, the mass-loss rates determined from blueshifted [O I] emission for the 12 stars that we associate with either extreme wind-dominated or accretion-dominated BC emission (those with blueshifted centroids in excess of -30 km s^{-1} or redshifted centroids in excess of 8 km s^{-1}) are all at the high end of classical T Tauri star mass-loss rates, with an average $\log \dot{M}_w = -8.3 \pm 0.7\ M_\odot\ \text{yr}^{-1}$, with no discernible difference between wind- and accretion-dominated objects. In contrast, those nine stars with NC-only helium emission tend to be those with predominately low velocity forbidden emission, and their average mass-loss rate is an order of magnitude smaller, with an average $\log \dot{M}_w = -9.7 \pm 0.7\ M_\odot\ \text{yr}^{-1}$. The fact that the mass-loss rate from the outer wind is comparably high in stars with accretion- or wind-dominated BC helium emission suggests that if there are two inner winds, whose relative strength is determined by a combination of the disk accretion rate and the stellar magnetic field strength, their combined mass-loss rate is comparable regardless of whether the hot or cool wind dominates. We infer that both will be collimated by the disk magnetic field and together form the outer collimated wind traced by blueshifted [O I].

9. SUMMARY AND CONCLUSIONS

Here we briefly recapitulate our analysis and conclusions. We have analyzed high-resolution emission-line profiles of

He I and He II in the spectra of 31 classical T Tauri stars. The high-excitation and ionization potentials of these lines make them a valuable diagnostic of hot gas in the star-disk interface region of disk-accreting stars. We find that helium emission likely arises in three distinct regions in classical T Tauri stars. A narrow component is attributed to formation in decelerating postshock gas emerging from the accretion shock at the magnetosphere/star boundary. A broad component is found to be composite with contributions from both magnetospheric infall and a hot wind.

The helium NC is characterized by relatively uniform line widths and slightly redshifted centroid velocities, although there are systematic differences among different lines, where He II λ4686 has the broadest FWHM (52 ± 8 km s^{-1}) and the largest redshift ($\mu_{\rm NC} = 10 \pm 5$ km s^{-1}). In contrast to helium, low-excitation metallic lines have NC line widths smaller by a factor of 2 and are at rest relative to the star, suggesting that NC emission properties will provide useful empirical constraints on postshock cooling models. The NC triplet-to-singlet ratio at He I, $I_{\lambda 5876}/I_{\lambda 6678}$, is a factor of 2 smaller than the nebular value, indicating that this component arises in a region of high density near thermal equilibrium.

The helium BC displays diverse kinematic properties, with centroid velocities ranging from blueshifts of -93 km s^{-1} to redshifts of 57 km s^{-1} and blue wing velocities ranging from -150 to at least -600 km s^{-1} at He I λ5876. A composite origin for the BC emission is required to explain the variety of profiles observed. Redshifted BC emission with $\mu_{\rm BC} > 8$ km s^{-1} (seen in seven stars) is most easily accounted for by restricting helium line formation to small polar angles in a funnel flow, where helium excitation would be provided by close proximity to ionizing radiation from the accretion shock. Blueshifted BC emission with $\mu_{\rm BC} < -30$ km s^{-1} (seen in seven stars) cannot result from infall in a funnel flow but instead likely arises from a hot wind suffering occultation of receding material by the star and disk. Similarly, BC helium blue wing velocities exceeding -200 km s^{-1} (seen in 14 stars) cannot be readily accounted for in funnel flows but have a natural explanation in outflowing gas. Although modest blueshifts can be produced in a funnel flow with emission over the full range of polar angles (MHC98), the fact that one-fourth of the objects in our sample have redshifted BC helium emission makes it problematic to have helium emission at small polar angles in some stars and at large polar angles in others. These points lead us to suggest that a major contributor to the BC helium emission is a hot wind.

We identify distinctly different behavior of the NC for stars with and without a hot helium wind, leading us to speculate on the origin of the hot wind and its relevance to other accretion/outflow indicators in classical T Tauri stars. We suggest that this hot wind emerges from polar regions in objects with some of the highest disk accretion rates. In those stars that lack any evidence for a hot wind, the NC flux correlates with both the (redshifted centroid) BC and the veiling, suggesting that in these stars magnetospheric accretion is responsible for all three phenomena. In those stars that do show evidence for a hot wind, the NC flux is not correlated with the (blueshifted centroid) BC or the veiling. We interpret this as evidence that the nature of the magnetospheric accretion shock, traced by the NC, is altered in those stars with hot winds in such a way that the luminosity and temperature of the shock are reduced. A possible scenario is that stars with either a high disk accretion rate or a weak magnetic field may crush the magnetosphere to the point where the disk can extend almost to the star and terminal velocities on short magnetic loops will be small. In this situation a wide polar/coronal wind could emerge from the accreting star, and Lyman continuum excess from hot coronal loops could excite the outflowing helium gas. An alternate source of optical veiling in this scenario could be provided by the magnetosphere/disk interaction region, where significant rotational energy would need to be dissipated before infall could occur.

The possibility that there might be multiple sources of optical veiling deserves some comment since veiling is the prime means of evaluating the accretion luminosity and thus the mass accretion rate for classical T Tauri stars. The earliest disk models attributed the veiling to dissipation of rotational energy in a viscous boundary layer at the stellar equator (Lynden-Bell & Pringle 1974), with a luminosity equal to $0.5GM_* \dot{M}/R_*$. This suggestion has since been superseded by the magnetospheric model, where the veiling is attributed to the dissipation of energy by infalling material on the stellar surface at the magnetic footpoints at a rate proportional to $(GM_* \dot{M}/R_*)(1 - R_*/R_t)$, where R_t is the truncation radius (Calvet & Gullbring 1998). The truncation radii have usually been taken to be large enough that most of the gravitational potential energy of the accreting matter is assumed to be radiated by the accretion shock (Calvet, Hartmann, & Strom 2000). In our scenario with a composite origin for the optical veiling, the basic proportionality between veiling luminosity and gravitational potential energy is preserved so that the current accretion estimates for classical T Tauri stars would not be altered significantly.

Analysis of the wing asymmetries in simultaneous Hα profiles indicates that there may be a contribution to Hα emission from the wind responsible for the blueshifted helium BC. Although one-third of the stars have symmetric wings at Hα, among those with asymmetric wings a blueward asymmetry is far more common than a redward asymmetry, after effects of P Cygni and inverse P Cygni absorption are accounted for. In particular, of the seven stars with BC helium blueshifted more than -30 km s^{-1}, five have blueward asymmetries in their Hα wings and two have deep P Cygni absorption below the continuum level beyond -200 km s^{-1}. We argue that this suggests a composite origin for Hα as well as for helium emission.

Examination of the blueshifted absorption at Hα attributed to an inner wind and the blueshifted forbidden line emission attributed to extended collimated jets leads us to conclude that in many disk-accreting classical T Tauri stars there are two winds that originate in near-stellar regions. One is the hot wind that we suggest emerges from polar regions, which can become important in stars with high disk accretion rates . The other is a cooler wind, possibly emerging from the inner disk as a centrifugal wind. Both inner winds would derive their energy from the accretion process and will be collimated by the disk magnetic field and together form the outer collimated wind traced by blueshifted [O I] λ6300.

The presence of a hot helium wind in disk-accreting T Tauri stars is inferred on the basis of the kinematic properties of the BC helium emission. The kinematic properties of He I profiles in the AeBe star AB Aur have also recently been interpreted as arising partly in outflowing gas,

although the profiles in this young intermediate-mass star do not closely resemble those in the low-mass stars under investigation here (Bouret & Catala 2000). We suggest here two ways in which our hypothesis for hot winds in classical T Tauri stars could be tested. One possibility would be to include high S/N helium profiles in long-term synoptic monitoring programs. The helium lines are much easier than Balmer lines to decompose, and if their BC emission has a composite origin, the wind and accretion contributions should exhibit different variability. Another prediction is that the hot polar/coronal wind, when present, will have a large excess in the Lyman continuum that should distinguish these stars from those with predominantly cool winds.

We acknowledge insightful conversations and constructive criticism from Lee Hartmann, Chris Johns-Krull, James Muzerolle, Nuria Calvet, Pat Hartigan, and Eugene Tademaru. Most of the veiling determinations and residual profiles were provided by Patrick Hartigan. Lee Hartmann, John Stauffer, and Steve Strom were collaborators in the acquisition of the spectra reported here. This work is based on the Ph.D. thesis of G. Beristain, who thanks David Kendall for his support and assistance.

REFERENCES

Alencar, S., & Basri, G. 2000, AJ, 119, 1881
Appenzeller, I., Jankovics, I., & Jetter, R. 1986, A&AS, 64, 65
Appenzeller, I., Reitermann, A., & Stahl, O. 1988, PASP, 100, 815
Athay, R. G. 1965, ApJ, 142, 755
Avrett, E. H., Vernazza, J. E., & Linsky, J. L. 1976, ApJ, 207, L199
Batalha, C. C., Stout-Batalha, N. M., Basri, G., & Terra, M. A. O. 1996, ApJS, 103, 211
Beristain, G., Edwards, S., & Kwan, J. 1998, ApJ, 499, 828
Bertout, C. 1989, ARA&A, 27, 351
Boesgaard, A. M. 1984, AJ, 89, 1635
Bouret, J. C., & Catalha, C. 2000, A&A, 359, 1011
Bouvier, J., Cabrit, S., Fernández, M., Martín, E. L., & Mathews, J. M. 1993, A&A, 272, 176
Brocklehurst, M. 1972, MNRAS, 157, 211
Calvet, N. 1997, in IAU Symp. 182, Herbig Haro Flows and the Birth of Low-Mass Stars, ed. B. Reipurth & C. Bertout (Dordrecht: Kluwer), 417
Calvet, N., & Gullbring, E. 1998, ApJ, 509, 802
Calvet, N., & Hartmann, L. 1992, ApJ, 386, 239
Calvet, N., Hartmann, L., & Hewett, R. 1992, ApJ, 386, 229
Calvet, N., Hartmann, L., Hewett, R., Valenti, J., Basri, G., & Walter, F. 1996, in ASP Conf. Proc. 109, Cool Stars, Stellar Systems, and the Sun, ed. R. Pallavicini & A. Dupree (San Francisco: ASP), 419
Calvet, N., Hartmann, L., & Strom, S. E. 2000, in Protostars and Planets IV, ed. V. Mannings, A. Boss, & S. S. Russell (Tucson: Univ. Arizona Press), 377
Camenzind, M. 1997, in IAU Symp. 182, Herbig Haro Flows and the Birth of Low-Mass Stars, ed. B. Reipurth & C. Bertout (Dordrecht: Kluwer), 241
Decampli, W. M. 1981, ApJ, 244, 124
Edwards, S. 1997, in IAU Symp. 182, Herbig Haro Flows and the Birth of Low-Mass Stars, ed. B. Reipurth & C. Bertout (Dordrecht: Kluwer), 433
Edwards, S., et al. 1993a, AJ, 106, 372
Edwards, S., Hartigan, P., Ghandour, L., & Andrulis, C. 1994, AJ, 108, 1056
Edwards, S., Ray, T., & Mundt, R. 1993b, in Protostars and Planets III, ed. E. H. Levy & J. I. Lunine (Tucson: Univ. Arizona Press), 567
Folha, D. F. M., & Emerson, J. P. 2001, A&A, 365, 90
Guenther, E. W., Lehmann, H., Emerson, J. P., & Staude, J. 1999, A&A, 341, 768
Gullbring, E., Hartmann, L., Briceno, C., & Calvet, N. 1998, ApJ, 492, 323
Hamman, F., & Persson, S. E. 1992, ApJS, 82, 247
Hartigan, P., Edwards, S., & Ghandour, L. 1995, ApJ, 452, 736 (HEG95)
Hartigan, P., Hartmann, L., Kenyon, S., Strom, S. E., & Skrutskie, M. F. 1990, ApJ, 354, L25
Hartmann, L., Hewett, R., & Calvet, N. 1994, ApJ, 426, 669 (HHC94)
Heasley, J. N., Mihalas, D., & Poland, A. I. 1974, ApJ, 192, 181
Hirth, G., Mundt, R., & Solf, J. 1997, A&AS, 126, 437
Johns, C., & Basri, G. 1995, AJ, 109, 2800
Johns-Krull, C. M., & Basri, G. 1997, ApJ, 474, 433
Johns-Krull, C. M., & Valenti, J. A. 2000, in ASP Conf. Ser. 198, Stellar Clusters and Associations: Convection, Rotation, and Dynamos, ed. R. Pallavicini, G. Micela, & S. Sciortino (San Francisco: ASP), 371
Johns-Krull, C. M., Valenti, J. A., Hatzes, A. P., & Kanaan, A. 1999a, ApJ, 510, L41
Johns-Krull, C. M., Valenti, J. A., & Koresko, C. 1999b, ApJ, 516, 900
Königl, A. 1991, ApJ, 370, L39
Königl, A., & Pudritz, R. 2000, in Protostars and Planets IV, ed. V. Mannings, A. Boss, & S. S. Russell (Tucson: Univ. Arizona Press), 759
Kwan, J., & Tademaru, E. 1988, ApJ, 332, L41
———. 1995, ApJ, 454, 382
Lamzin, S. A. 1989, AZh, 66, 1330
Lynden-Bell, D., & Pringle, J. E. 1974, MNRAS, 168, 603
Mitskevich, A. S., Natta, A., & Grinin, V. P. 1993, ApJ, 404, 751
Muzerolle, J., Calvet, N., & Hartmann, L. 1997, ApJ, 492, 743
———. 2001, ApJ, 550, 944
Muzerolle, J., Hartmann, L., & Calvet, N. 1998, AJ, 116, 455 (MHC98)
Najita, J., Edwards, S., Basri, G., & Carr, J. 2000, in Protostars and Planets IV, ed. V. Mannings, A. Boss, & S. S. Russell (Tucson: Univ. Arizona Press), 457
Osterbrock, D. E. 1974, Astrophysics of Gaseous Nebulae (San Francisco: Freeman)
Press, W. H., Teukolsky, S. A., Vetterling, W. T., & Flannery, B. P. 1992, Numerical Recipes in C: The Art of Scientific Computing (2d ed.; New York: Cambridge Univ. Press)
Schneeberger, T. J., Linsky, J. L., & Worden, S. P. 1978, A&A, 62, 447
Shu, F. H., Najita, J., Ostriker, E., Wilken, F., Ruden, S., & Lizano, S. 1994, ApJ, 429, 781
Shu, F., Najita, J., Shang, H., & Li, Z. 2000, in Protostars and Planets IV, ed. V. Mannings, A. Boss, & S. S. Russell (Tucson: Univ. Arizona Press), 789
Smits, D. P. 1991, MNRAS, 248, 193
———. 1996, MNRAS, 278, 683
Uchida, Y., & Shibata, K. 1985, PASJ, 37, 515
Ulrich, R. K., & Wood, B. C. 1981, ApJ, 244, 147
Wahlstrom, C., & Carlsson, M. 1994, ApJ, 433, 417
Zirin, H. 1975, ApJ, 199, L163